



## Predicted bounds on peak global mean sea level during marine isotope stages 5a and 5c



Jessica R. Creveling <sup>a,\*</sup>, Jerry X. Mitrovica <sup>b</sup>, Peter U. Clark <sup>a</sup>, Claire Waelbroeck <sup>c</sup>, Tamara Pico <sup>b</sup>

<sup>a</sup> Oregon State University, College of Earth, Ocean, and Atmospheric Sciences, 104 CEOAS Administration Building, Corvallis, OR 97331, USA

<sup>b</sup> Harvard University, Earth and Planetary Sciences, 20 Oxford Street, Cambridge, MA 02138, USA

<sup>c</sup> Laboratoire des Sciences du Climat et de l'Environnement, LSCE/IPSL, Laboratoire CNRS-CEA-UVSQ, Domaine du CNRS, bât 12, 91198, Gif-sur-Yvette, France

### ARTICLE INFO

#### Article history:

Received 23 October 2016

Received in revised form

2 March 2017

Accepted 3 March 2017

Available online 3 April 2017

#### Keywords:

Quaternary

MIS 5

Global

Sea-level changes

Numerical modeling

Glacial isostatic adjustment

Geomorphology

Coastal

Glaciology (paleo-ice sheets)

### ABSTRACT

Estimates of marine isotope stage (MIS) 5c and 5a global mean sea level (GMSL) based on marine terraces and coastal indicators range from 15–37 m and 9–30 m below present, respectively. Tectonic displacement and glacial isostatic adjustment (GIA) complicate efforts to refine this range. We revisit this issue using numerical predictions of post-glacial sea-level change and updated estimates of site-specific tectonic signals based upon these predictions. Laurentide and Cordilleran peripheral bulge dynamics and variations in the gravitational effect of these ice masses dominate the GIA signal along the east and west coasts of North America. Published compilations suggest that MIS 5 sea-level indicators extending from Virginia to the Caribbean lie on the outer flank of the peripheral bulge, while those along a transect from Oregon to Baja California sit on the inner flank of the bulge. Our GIA modeling reconciles these data by adopting a significantly weaker (i.e., lower viscosity) upper mantle in analyzing data on the Pacific coast relative to the Atlantic, an inference supported by seismic tomography. We present a sensitivity analysis that compares the observed elevation of globally distributed high stand markers to a suite of GIA simulations that vary the Earth model and GMSL from the Last Interglaciation (MIS 5e, ~130–115 ka) to 70 ka. We conclude that GMSL peaked at  $-8.5 \pm 4.6$  m ( $1\sigma$ ) during MIS 5a and  $-9.4 \pm 5.3$  m during MIS 5c. A more restrictive analysis yields slightly wider bounds corresponding to  $-10.5 \pm 5.5$  m and  $-11.1 \pm 6.6$  m, respectively.

© 2017 Elsevier Ltd. All rights reserved.

### 1. Introduction

Benthic oxygen isotope records and dated corals indicate that the transition from the Last Interglaciation (LIG, ~130–115 ka) and associated marine isotope (MIS) stage 5e to the Last Glacial Maximum (26–19 ka, MIS 2) was punctuated by several large fluctuations in ice-sheet volume and associated sea level (Chappell and Shackleton, 1986; Lambeck and Chappell, 2001; Cutler et al., 2003). Understanding the timing and amplitude of these fluctuations is important for assessing ice-sheet sensitivity to climate change, but constraints on their age and amplitude remain uncertain. Based on dating of raised coral-reef terraces on Barbados, Broecker et al. (1968) and Mesolella et al. (1969) first determined that the two sea-level high stands immediately following the LIG, corresponding

to MIS 5c and 5a, correlate with Northern Hemisphere summer insolation maxima at ~100 ka and ~80 ka, respectively, thereby providing early evidence for the astronomical theory of ice ages (Milankovitch, 1938). As summarized below, there is now considerable evidence around the world for these high stands, but estimates of their associated peak global mean sea level (GMSL) differ by tens of meters.

A common method for estimating ice-volume fluctuations and the associated variations in 'eustatic' or GMSL involves correcting benthic oxygen isotope ( $\delta^{18}\text{O}$ ) records for temperature in order to isolate that part of the signal that reflects ice volume (Chappell and Shackleton, 1986; Waelbroeck et al., 2002; Elderfield et al., 2010). However, additional complexities such as time dependence in the isotopic composition of ice sheets and spatial heterogeneities in the isotopic signature of seawater also hinder the mapping of  $\delta^{18}\text{O}$  to eustatic sea level (Mix, 1987; Clarke and Marshall, 2002; Waelbroeck et al., 2002; Siddall et al., 2008). Moreover, many

\* Corresponding author.

E-mail address: [jcreveling@ceoas.oregonstate.edu](mailto:jcreveling@ceoas.oregonstate.edu) (J.R. Creveling).

$\delta^{18}\text{O}$  records are not directly dated beyond the range of radiocarbon (~40 ka), and thus rely on other dating strategies (Huybers and Wunsch, 2004; Lisiecki and Raymo, 2005) that introduce uncertainty in the age of inferred peak GMSL high stands.

Direct indicators of sea level, including geomorphic features and sedimentological records, also provide important constraints on past sea-level change. Unlike  $\delta^{18}\text{O}$  records, these indicators can be dated directly, but such records are discontinuous in both time and space. Mapping the present elevations of these local sea-level indicators to GMSL requires a correction for local tectonic uplift/subsidence (e.g., Bloom et al., 1974; Dodge et al., 1983; Ota and Omura, 1992; Lambeck and Chappell, 2001; Gallup et al., 2002; Murray-Wallace, 2002; Dumas et al., 2006; Muhs et al., 2012; Creveling et al., 2015; and many others), steric and ocean dynamic effects (e.g., McKay et al., 2011) and glacial isostatic adjustment (GIA), where the latter includes the full suite of deformational, gravitational, and rotational effects resulting from changing Quaternary ice and ocean loads (Lambeck and Chappell, 2001; Potter and Lambeck, 2003; Raymo and Mitrovica, 2012; Dutton and Lambeck, 2012; Muhs et al., 2012; Chen et al., 2013; Hay et al., 2014; Creveling et al., 2015; Simms et al., 2015).

Previous studies of the MIS 5a and 5c high stands highlighted the importance of the GIA correction in establishing rigorous bounds on coeval GMSL. For instance, peak high-stand elevations across the southeastern U.S. Atlantic coastal plain and Caribbean display a strong latitudinal gradient, decreasing in elevation by ~30 m (Cronin et al., 1981; Szabo, 1985; Bard et al., 1990; Cutler et al., 2003; Potter and Lambeck, 2003; Potter et al., 2004; Wehmiller et al., 2004; Parham et al., 2013). Potter and Lambeck (2003) demonstrated that this gradient reflects the differential effect of GIA on ‘near-field’ sites located on the peripheral bulge of the Laurentide Ice Sheet (LIS). After correction for this signal, Potter and Lambeck (2003) concluded that GMSL during MIS 5a peaked at ~28 m below present, and reached a similar value during MIS 5c. Lambeck and Chappell (2001) found that, after correcting coral-reef terrace elevations on the Huon Peninsula, Papua New Guinea, for tectonic and GIA effects, peak GMSL during MIS 5a and 5c reached 23–37 m and 18–30 m below present, respectively. In contrast, Muhs et al. (2012) reported that, after correcting for tectonic and GIA effects, MIS 5a and MIS 5c high stands on San Nicolas Island, California; the Florida Keys; and Barbados reveal peak GMSL of −16 m during MIS 5a and −9 m during MIS 5c. Simms et al. (2015) extended the analysis by Muhs et al. (2012) by considering 30 sites along the Pacific coast of the U.S. and Mexico that are characterized by a strong gradient in local high-stand elevations during MIS 5a and MIS 5c. After correcting for tectonic and GIA effects, they concluded that GMSL was −15 m and −10 m during MIS 5a and 5c, respectively, in agreement with Muhs et al. (2012).

Estimates of MIS 5a and 5c GMSL from sea-level indicators that account for GIA and tectonics thus range from 15–37 m below present and 9–30 m below present, respectively, and do not provide statistical bounds on the uncertainty of reconstructed GMSL. Here we extend previously published, regional reconstructions of MIS 5a and 5c peak high-stand elevations in two ways. First, we present global maps of the GIA contribution to MIS 5a and MIS 5c peak sea level. Using these global maps to make site-specific predictions of relative sea level (RSL), we summarize the dominant physical controls on the amplitude and spatial variability of the predicted high stands. Second, we present a large suite of GIA predictions and compare these to previously published, globally distributed observations in order to derive rigorous bounds (with associated uncertainty) on peak GMSL achieved during the MIS 5a and MIS 5c high stands.

## 2. Summary of paleo sea-level data

We compiled published elevation measurements of local MIS 5a and 5c RSL from 38 sites distributed around the globe (Table 1). These sites include, but are not limited to, those compiled by Simms et al. (2015) for the Pacific Coast of the United States and Baja California Sur, Mexico and by Potter and Lambeck (2003) for the U.S. southeast Atlantic coast and Caribbean. The sea-level indicators include wave-cut terraces, erosional notches, shoreface lithofacies, bio-/ichno-facies, coral-reef crests, and speleothems (Murray-Wallace and Woodroffe, 2014; Rovere et al., 2016). These proxies variably provide minimum, maximum, and bounded constraints on former sea level.

For geomorphic features such as uplifted terraces, the intersection of the wave-cut bench and the steep-faced sea cliff, called the shoreline angle, closely constrains the former shoreline (Muhs et al., 2012). Similarly, notches reflect erosion and/or dissolution of terraces and sea cliffs by wave and tidal dissipation, or biological erosion, and thus bound the paleo-intertidal range (Focke, 1978; Pirazzoli, 1986). Reef-crest corals form topographic highs above backreef (lagoonal) environments and deeper, forereef corals. Reef-crest elevations thus provide bounds on paleo-sea level with uncertainties comparable to the depth of the modern ecological growth range of the relevant coral species (Goreau, 1959; Mesolella et al., 1970; Lighty et al., 1982). For example, the reef-crest coral *Acropora palmata* is usually found within the upper 6 m of the water column in the western Atlantic Ocean when sea level is not changing (Goreau, 1959). Litho-, bio- and ichnofacies indicative of subaerial environments provide maximum constraints on paleo-sea level, whereas facies characteristic of subaqueous environments provide either a minimum constraint or bound sea level with an uncertainty equal to the water depth at the seaward limit of the facies belt (Rovere et al., 2016). Finally, speleothems aggrade under subaerial conditions and cease growth when transgressing seas inundate caves, thus providing a maximum constraint on paleo-sea level at the time of carbonate nucleation (Richards et al., 1994).

The present elevation of MIS 5 paleo sea-level indicators may reflect some displacement by tectonics. The most common method for applying a tectonic correction involves comparing observed MIS 5e high-stand elevation records at a site to peak GMSL during MIS 5e. This method has traditionally assumed a globally uniform and fixed value for MIS 5e sea level, often +6 m, and thus it does not account for the potential error in the adopted GMSL value or the spatial variability in sea level during MIS 5e due to GIA (Kopp et al., 2009; Creveling et al., 2015). Where possible, we report the present elevation of sea-level indicators, and not the tectonically corrected datums, in order to apply recently revised, site-specific corrections for tectonic uplift and GIA to each site in the data set (Table 1; Hay et al., 2014; Creveling et al., 2015). (We report relevant uncertainties separately in Table 1.) In the following summary, unless otherwise indicated, the reconstructed sea levels that we cite have been corrected for growth/depositional depth uncertainty and tectonic effects by the primary authors and represent local RSL values, rather than GMSL.

### 2.1. Pacific Coast of North America

Simms et al. (2015) tabulated the present elevations of MIS 5 shoreline markers at 30 Pacific coastal sites extending from northern Oregon, U.S.A. to the southern tip of Baja California Sur, Mexico. We confine our analysis to the subset of these sites with an MIS 5e and an MIS 5a and/or 5c paleo-shoreline marker (Table 1, sites 1–20 and 37). However, there are several issues to note regarding some of the sites included within this database. For instance, one or more of the reported MIS 5 terraces at sites 1–6,

**Table 1**

Field localities, age assignments, and elevations of geological markers adopted in this study. See references for details of measurement procedure and discussion of error. Site numbers and field localities highlighted in bold represent the subset of terrace elevations adopted for the more restrictive Monte Carlo analysis discussed in the text and presented in Fig. 11.

Site number	Field locality	Marine Isotope Stage (MIS)	Elevation (m)	Uncertainty (m) <sup>a</sup>	References
1	Newport, OR	5a	45	3.3	Kennedy et al. (1982);
		5c	85	6	Kelsey et al. (1996)
		5e	109	6	
2	Cape Arago, OR	5a	31	6	Adams (1984);
		5c	68	6	McInelly and Kelsey (1990)
		5e	98	6	
3	<b>Coquille Point, OR</b>	5a	45	5	Kennedy et al. (1982);
		5c	70	5	McInelly and Kelsey (1990);
		5e	105	5	Muhs et al. (1990) and (2006)
4	Brookings, OR	5a	53	9	Kelsey and Bockheim (1994)
		5c	77	9	
		5e	111	9	
5	Bruhel Point, CA	5a	10	2	Merritts and Bull (1989)
		5c	23	2	
		5e	40	2	
6	Point Reyes, CA	5a	77	1	Grove et al. (2010)
		5e	142	1	
7	Santa Cruz, CA	5a	87	3.3	Anderson and Menking (1994);
		5c	132	3.3	Perg et al. (2001)
		5e	170	3.3	
8	San Simeon, CA	5a	9	2	Hanson et al. (1992);
		5e	25	1	Berger and Hanson (1992)
9	Point Buchon, CA	5a	11	3	Hanson et al. (1992)
		5e	30	4	
10	Gaviota, CA	5a	13	5	Rockwell et al. (1992)
		5c	25	5	
		5e	35	5	
11	<b>Santa Rosa Island, CA</b>	5a	7.4	1	Muhs et al. (2014) and (2015)
		5e	24	1	
12	San Miguel Island, CA	5a	3.5	5	Muhs et al. (2014)
		5e	22.5	1.5	
13	<b>Palos Verdes Hills, CA</b>	5a	40	4	Muhs et al. (1992) and (2006)
		5e	75	4	
14	San Joaquin Hills, CA	5a	20.5	1.5	Grant et al. (1999)
		5e	34	2	
15	<b>San Nicolas Island, CA</b>	5a	10	3	Muhs et al. (2006) and (2012)
		5c	30.7	2	
		5e	36	2	
16	Oceanside, CA	5a	9	2	Kern and Rockwell (1992)
		5e	22	2	
17	<b>Point Loma, CA</b>	5a	8	2	Ku and Kern (1974); Kern and Rockwell (1992); Muhs et al. (1992)
		5e	23	2	
18	<b>Punta Banda, Mexico</b>	5a	16	2	Rockwell et al. (1989);
		5c	22	2	Muhs et al. (2002a)
		5e	35.5	2	
19	Punta Cabras, Mexico	5a	6	2	Addicott and Emerson (1959);
		5e	17	2	Mueller et al. (2009)
20	Turtle Bay, Mexico	5a	12	1	Emerson et al. (1981)
		5e	25.5	1.5	
21	Virginia Beach (Gomez Pit), VA	5a	6.5	3.5	Crонин et al. (1981); Szabo (1985); Wehmiller et al. (2004)
22	Moyock, NC	5a	5	3	Wehmiller et al. (2004)
23	Pamlico Sound, NC	5a	9	3	Parham et al. (2013)
24	Charleston, SC	5a	6.5	3.5	Cronin et al. (1981); Szabo (1985); Wehmiller et al. (2004)
25	Skidaway Island, GA	5a	3	3	Cronin et al. (1981); Szabo (1985); Wehmiller et al. (2004)
26	<b>Fort St. Catherine, Bermuda</b>	5a	1	1	Ludwig et al. (1996);
		5e	5	1	Muhs et al. (1992)
27	<b>Sand Key Reef, FL</b>	5a	-8	2	Ludwig et al. (1996); Toscano and Lundberg (1999)
		5e	4	1	
28a	Eleuthera Is., Bahamas	5a	-2.5	2.5	Hearty and Kaufman (2000)
28b	Grand Bahama Is., Bahamas	5a	-18.1	—	Richards et al. (1994)
28c	<b>Berry Islands, Bahamas</b>	5c	1	1	Neumann and Moore (1975)
		5e	2.3	NR	
29	<b>Northwestern Peninsula, Haiti</b>	5a	23.4	—	Dodge et al. (1983);
		5c	37.2	—	Dumas et al. (2006)
30a	<b>Christ Church Traverse, Barbados</b>	5a	60.7	—	Bender et al. (1979);
		5c	3	+1/-2	Edwards et al. (1997)
30b	<b>Clermont Nose Traverse, Barbados</b>	5c	6	+5/-1	
		5e	37	2	
30b	<b>Clermont Nose Traverse, Barbados</b>	5a	20	3	Bender et al. (1979);
		5c	30	3	Edwards et al. (1997)

(continued on next page)

**Table 1** (continued)

Site number	Field locality	Marine Isotope Stage (MIS)	Elevation (m)	Uncertainty (m) <sup>a</sup>	References
31	Bahía Inglesa, Chile	5e	61	2	
		5a	10	5	
		5c	31	5	
		5e	40	5	
32	Daebo-Gori region, Korea	5a	9.5	1.5	
		5c	19.5	2.5	
		5e	29	4	
		5a	3.5	1	
33a	<b>Pamalican Is., Philippines</b>	5c	10.5	1.6	
		5e	26.8	—	
		5c	5	NR	
33b	Panglao Is., Philippines	5e	7.5	0.4	
		5a	260	NR	
		5c	338	NR	
		5e	440	NR	
34a	<b>Huon Peninsula, Papua New Guinea (Tewai section)</b>	5a	117	NR	
		5c	160	NR	
		5e	220	NR	
		5a	23	2	
35	<b>Hateruma Island, Ryukyu Is., Japan</b>	5c	30	2	
		5e	41	2	
		5a	20	NR	
		5c	36	NR	
36	<b>Atauro Is., East Timor</b>	5e	63	NR	
		5a	55	5	
		5c	37	5	
		5e	—2	NR	
37	Malibu, CA	5c	10	NR	
		5e	NR		
38	Spencer Gulf, Australia	5c	NR		
		5e	NR		

— = Assumed negligible, NR = Not reported.

<sup>a</sup> Elevation errors for Sites 1–20 adopted from Simms et al. (2015).

8–10, 12, 16, and 19 lack a direct age, and their assigned MIS 5 age is based largely on its elevation relative to other terraces, with the lowest often assumed to represent MIS 5a. Accepting the age assignments for these undated terraces, no matter how well reasoned, introduces uncertainty to any calculation of MIS 5a and 5c sea level. Other authors defer to ages from nearby field localities. For instance, Grant et al. (1999) reported robust MIS 5e ages and a possible MIS 5c age based on dated corals from two emergent terraces at San Joaquin Hills, CA (site 14). However, the authors argued that the elevation of this terrace better corresponds to MIS 5a terrace elevations reported elsewhere in southern California (e.g., Muhs et al., 1994). Grant et al. (1999) concluded that the MIS 5c coral must represent an allochthonous fragment reworked into the MIS 5a terrace, or that corals representing both high stands occupied the same terrace. The reported  $2\sigma$  age uncertainty for some sites precludes a distinction between MIS 5a and 5c high stands. At Point Loma, CA (site 17), corals sampled from the 23 m terrace display open system behavior, and show clustered ages consistent with both MIS 5e and 5c sea level high stands (Muhs et al., 2002a). Hence the assignment of this terrace to MIS 5e by Simms et al. (2015) remains uncertain. Emerson et al. (1981) reported amino acid racemization (AAR) ages on fossil mollusks sampled from a terrace at Turtle Bay, Baja California Sur, Mexico (site 20), that range from 65 to 95 ka. Similar uncertainty exists for U-series dates on mammal teeth and bone fragments interpreted as minimum ages for putative MIS 5a terraces at San Simeon, CA and Point Buchon, CA (sites 8 and 9; Berger and Hanson, 1992; Hanson et al., 1992).

Two of the sites from the Simms et al. (2015) database include radiometric constraints that have been questioned in the literature. At Santa Cruz, CA (site 7), Perg et al. (2001) reported MIS 5 cosmogenic ages that were contested by Muhs et al. (2006), who speculated that the ages constrain the deposition of alluvium overlying the marine terraces, and should thus provide a minimum

age on the date of terrace formation. At Malibu, CA (site 37), Birkeland (1972) and Szabo and Rosholt (1969) reported U-series dates from mollusk shells from purported MIS 5 terraces, though such ages commonly differ from independent radiometric constraints and do not provide robust age assignments (Kaufman et al., 1971).

Of the remaining sites adopted from the compilation by Simms et al. (2015), Santa Rosa Island, CA (site 11; Muhs et al., 2014, 2015), Palos Verdes Hills, CA (site 13; Muhs et al., 1992, 2006), and Punta Banda, Mexico (site 18; Rockwell et al., 1989; Muhs et al., 1992) include U-series dates on both MIS 5a and 5e terraces. Robust U-series dates assign three terraces at San Nicolas Island, CA (site 15; Muhs et al., 2006, 2012) to MIS 5a, 5c and 5e.

## 2.2. U.S. Atlantic coastal plain and Caribbean

The elevations of MIS 5a coral-bearing estuarine, intertidal, and subtidal lithofacies on the U.S. Atlantic coastal plain—extending from Virginia south to Georgia—vary from ~0 to +12 m above present sea level (Table 1, sites 21–25). However, these sites lack paired MIS 5e terraces for site-specific assessments of tectonic displacement (Cronin et al., 1981; Wehmiller et al., 2004; Murray-Wallace and Woodroffe, 2014). Under the assumption of negligible tectonic uplift between MIS 5e and the present, the present elevations of U.S. Atlantic coastal plain terraces indicate that MIS 5a RSL peaked 3–12 m above present (e.g., Potter and Lambeck, 2003; Parham et al., 2013).

The Bermudan record of MIS 5a sea level remains controversial. While coral-bearing marine lithofacies at present elevations of +1–2 m may indicate an MIS 5a RSL of 0–2 m (Table 1, site 26; Harmon et al., 1983; Vacher and Hearty, 1989; Ludwig et al., 1996; Muhs et al., 2002b), a stalagmite sampled 15 m below sea level in Crystal Cave, Bermuda, alternatively suggests that MIS 5a sea level did not reach this elevation (Harmon et al., 1983). Wainer et al.

(2017) reported hiatuses in the growth of a stalactite from Wilkinson Quarry Cave, northern Bermuda, which indicates that local sea level peaked above ~1.5 m during MIS 5e, 5c, and 5a, consistent with the lithofacies indicators discussed above.

At Carysfort Outlier Reef, Florida, Toscano and Lundberg (1999) reported an *A. palmata* reef-crest coral from a drill core recovered at 15.2 m below present sea level. They applied a subsidence correction to derive an elevation of  $-13.9 \pm 0.3$  m, and then corrected for a paleo-growth depth of 5 m to estimate that MIS 5a sea level reached a maximum of  $-8.9 \pm 0.3$  m. Toscano and Lundberg (1999) also reported an *M. annularis* coral from a drill core at 12.3 m below present sea level at Sand Key Outlier Reef, lower Florida Keys. Applying the same subsidence rate and assuming a reef-crest growth elevation of 2–3 m water depth, they estimated a maximum MIS 5a sea level of  $-6.1 \pm 1.5$  m, consistent with the  $-8 \pm 1$  m lower bound on peak MIS 5a sea level for the same site estimated by Ludwig et al. (1996). Potter and Lambeck (2003) appear to have combined the peak high-stand elevations reported by Toscano and Lundberg (1999) for the Carysfort and Sand Key Outlier reefs, and cited a range of  $-8 \pm 2$  m for the Florida Keys. We adopt this range in our analysis (Table 1, site 27).

Hearty and Kaufman (2000) reported Couplet V limestone eolianite lithofacies between 0 and –5 m elevation at Eleuthera Island, Bahamas and, based on whole-rock AAR ages, reconstructed MIS 5a local sea level between these bounds (Table 1, site 28a). In contrast, Richards et al. (1994) and Toscano and Lundberg (1999) reported a speleothem 18.1 m below present sea level at Grand Bahama Island that, given an assumed subsidence correction, would imply that local MIS 5a sea level was no higher than  $-16.5 \pm 0.1$  m (Table 1, site 28b). Neumann and Moore (1975) reported U-series dates on two *Diploria labyrinthiformis* samples from Goat Cay and Cockroach Cay, Berry Is., Bahamas, at elevations of  $+1.5$  m ( $103 \pm 5$  kyr) and  $+1.0$  m ( $105 \pm 5$  kyr), respectively, and a *Diploria strigosa* sample from Lignum Vitae Cay, Berry Is. at 0.8 m ( $94 \pm 8$  kyr, and a rerun age of  $112 \pm 6$  kyr). We adopt an elevation range of  $1 \pm 1$  m and age  $104 \pm 5$  kyr for this site (Table 1, Site 28c). A U-series date of  $132 \pm 7$  kyr on a fragment of *Monastrea annularis* sampled 2.3 m above present sea level indicates that MIS 5e paleo-sea level reached that height (Neumann and Moore, 1975). Given the inconsistent estimates, we excluded the Bahamian speleothem and eolianite data from our analysis constraining peak GMSL during MIS 5a, although we compare our best-fit predictions to these data (see below).

On Grand Cayman Island, British West Indies, Coyne et al. (2007) reported unconformity bound sedimentary packages interpreted to record deposition during MIS 5e, 5c, and 5a based on U/Th ages from corals and conch shells (*Strombus gigas*). Assuming tectonic stability, and correcting for biological range depths of *Strombus gigas* (MIS 5a) and *Conichnus* and *Ophiomorpha* trace fossils (MIS 5c), Coyne et al. (2007) concluded that RSL during MIS 5c and 5a peaked ~3–5 m and ~3–6 m, respectively, above present sea level. Murray-Wallace and Woodroffe (2014) questioned the fidelity of the indicative range of the biofacies-based paleo-sea level indicators for both the MIS 5a and 5c stratigraphic units presented by Coyne et al. (2007), and for this reason we excluded this site from our analysis of MIS 5a and 5c peak GMSL.

Dumas et al. (2006) revised the geochronological and elevation constraints on Haitian MIS 5e, 5c, and 5a terraces reported by Dodge et al. (1983). Once corrected for tectonic effects (using an assumed MIS 5e high-stand elevation) and coral growth ranges, this yielded estimates of MIS 5c sea level of  $-8 \pm 2$  m and MIS 5a sea level of  $-11 \pm 2$  m (Table 1, site 29).

Elevation measurements and geochronological analyses on MIS 5e, 5c, and 5a Barbados coral-reef terraces have been reported and refined several times (cf. Broecker et al., 1968; Mesolella et al., 1969;

Bender et al., 1979; Bard et al., 1990; Cutler et al., 2003; Potter et al., 2004). Bender et al. (1979) presented elevation measurements for MIS 5a, 5c, and 5e terraces of 3 m, 6 m, and 37 m, respectively, for the Christ Church Traverse, and 20 m, 30 m, and 61 m, respectively, for the Clermont Nose Traverse (Table 1, sites 30a and 30b, respectively). Edwards et al. (1997) confirmed the aforementioned age assignments with both  $^{230}\text{Th}/^{238}\text{U}$  and  $^{231}\text{Pa}/^{235}\text{U}$  dates.

### 2.3. Far-field localities

Marquardt et al. (2004) investigated a flight of uplifted Quaternary terraces at Bahía Inglesa, northern Chile (Table 1, site 31). The lowermost terraces, at elevations of  $10 \pm 5$  m,  $31 \pm 5$  m, and  $40 \pm 5$  m, were assigned to MIS 5a, 5c, and 5e, respectively, based on terrace counting and cool-water faunal associations. Given the circularity that arises from modeling peak GMSL with assigned marine isotope stages, we excluded Bahía Inglesa from our analysis of MIS 5a and 5c peak GMSL. However, in the discussion below, we compare our best fit predictions to the Bahía Inglesa terrace elevations.

Choi et al. (2008) assigned inner-edge terraces from the Daebogori region, Korea, to MIS 5e, 5c, and 5a based on optically stimulated luminescence (OSL) ages on foreslope sand and alluvium overlying terrace surfaces (Table 1, site 32). After applying uplift corrections by assuming that peak MIS 5e high-stand elevations reached 3–6 m above present, and adopting idealized ages of 105 and 76–80 ka, they concluded that MIS 5c and 5a sea level peaked at 5 and 10 m below present sea level, respectively.

Ringor et al. (2004) reported U-Th ages on coral terraces from Pamalican Island, Philippines, that suggested formation during MIS 5a, 5c, and 5e (Table 1, site 33a). Assuming constant rates of uplift and an MIS 5e paleo-sea level of 3–6 m, the authors estimated that MIS 5a and 5c sea levels peaked between –6 and –9 m, and –9 to –11 m, respectively. On the nearby island of Panglao, Omura et al. (2004) reported a terrace along the San Isidro coastline with two morphostratigraphic units (Table 1, site 33b). The lower unit includes a U-Th dated MIS 5e terrace with an inner margin situated 7.1–8 m above present sea level. Within this terrace, a *Porites* s. coral at ~3 m elevation is truncated by a younger, MIS 5c *Platygyra ryukyuensis* coral-bearing grainstone unit. Assuming a preferred growth depth for *P. ryukyuensis* of 0–2 m, the authors concluded that MIS 5c sea level peaked ~5 m above present sea level.

Unusually high rates of tectonic uplift across the Huon Peninsula, Papua New Guinea, facilitate the preservation of MIS 5a and 5c high stand coral terraces. Chappell and Shackleton (1986) reported MIS 5e, 5c and 5a coral reef crest elevations of 440 m, 338 m and 260 m (Tewai Section) and 220 m, 160 m and 117 m (Kwambu Section), respectively (Table 1, site 34). Assuming an MIS 5e high-stand elevation of 6 m at 124 ka, they reconstructed local MIS 5c and 5a sea levels of  $-9 \pm 3$  m and  $-19 \pm 5$  m, respectively.

Coral-reef terraces on Hateruma, Ryukyu Islands, Japan, can aide in constraining MIS 5a and 5c sea level (Table 1; site 35). In order to assess local variation in tectonic uplift, Ota and Omura (1992) compared the highest elevation of MIS 5e, 5c, and 5a shorelines, at  $41 \pm 2$  m,  $30 \pm 2$  m, and  $23 \pm 2$  m, respectively, to presumed coeval paleo-sea level heights reported by Chappell and Shackleton (1986), which inferred an MIS 5e sea level of 6 m.

U-Th ages suggest that uplifted terraces 1b and 2 on Atauro Island, East Timor, represent MIS 5c and MIS 5e sea level at present elevations of 36 and 63 m (Table 1, site 36; Chappell and Veeh, 1978). Terrace 1a, at ~20 m above present sea level, yielded no datable coral material but was assumed to record deposition during MIS 5a. Assuming that MIS 5e paleo-sea level peaked at  $6.5 \pm 0.5$  m, the terrace elevations from Atauro broadly constrain local peak MIS 5a and 5c sea level to –14 and –20 m, respectively (Chappell and

Veeh, 1978).

A succession of eolian barrier dunes crops out along the Coorong coastal plain, southern Australia, though the age constraints for the stranded units remain uncertain (Huntley et al., 1994). Murray-Wallace (2002) assigned the  $-2$  m elevation Robe III and  $+10$  m elevation Woakwine I eolinite deposits, previously dated by thermoluminescence to  $116 \pm 6$  kyr and  $132 \pm 9$  kyr (Huntley et al., 1994), to MIS 5c and 5e, respectively (Table 1, site 38). Assuming an MIS 5e paleo-sea level of 2 m, Murray-Wallace (2002) concluded that local MIS 5c sea level peaked 9 m below present.

Finally, we excluded two sites reporting local MIS 5 paleo-sea level because of the potential for systematic error in our GIA prediction. First, offshore of eastern Oahu, Hawaii, the submerged Waianae reef includes U-series dated *Porites lobata* representing aggradation at depths of 30 and 27 m below present sea level during MIS 5a and 5c, respectively (Sherman et al., 1999, 2014). Although *P. lobata* grows at depths down to 40 m, Sherman et al. (2014) reported a typical growth depth of 3–15 m. Muhs and Szabo (1994) reported elevations of an emergent MIS 5e-aged reefal unit, the Waimanalo Limestone, across Oahu and concluded that elastic flexure, while minimal, affects the present elevation of this LIG shoreline marker. A complication is that the viscosity below the hot-spot island is expected to be very low, and this may significantly impact a GIA prediction for this site. On this basis we have chosen to exclude the site from our analysis, as it requires modeling that captures this local 3-D viscosity structure.

Second, Simms et al. (2009) reported MIS 5a barrier-island facies, dated by optically stimulated luminescence ( $90.7 \pm 5.5$  ka), up to 18.9 m below present sea level within sediment cores from the Freeport Rocks Bathymetric High in the Gulf of Mexico. Assuming the beach formed 1–2 m above sea level, and correcting for subsidence of 0.01 cm/year, the authors estimated a local MIS 5a sea level high stand of no higher than  $-11 \pm 2$  m. However, previous studies have demonstrated that this location is sensitive to loading associated with sediment redistribution and for this reason we have chosen to omit the site from our analysis (Ivins et al., 2007; Simms et al., 2007; Dalca et al., 2013).

#### 2.4. Summary of the MIS 5 paleo-sea level indicators adopted in the statistical analyses

To accommodate the range of uncertainty in the present elevation of paleo-sea level indicators (including instrumental precision and various indicative ranges; Rovere et al., 2016) and the geochronology, we performed two statistical assessments of peak MIS 5c and 5a GMSL (see section 4.2). In the first, we adopted the majority of near and far field sites for which geological data constrain local relative sea level; for both MIS 5a and 5c, this included all sites except for the Bahamas (site 28A-C) and Bahía Inglesa, Chile (site 31). For the second analysis, we adopted a filtered dataset that emphasizes those sites with at least one robust U-series dated marker and narrow indicative ranges. For MIS 5a this includes only a subset of data from the Pacific and Atlantic coasts of North America, and the majority of far-field localities: Coquille Point, OR (site 3); Santa Rosa Island, CA (site 11); Palos Verdes Hills, CA (site 13); San Nicolas Island, CA (site 15); Point Loma, CA (site 17); Punta Banda, Mexico (site 18); Bermuda (site 26); Sand Key Reef, FL (site 27); Haiti (site 29); Barbados (sites 30A and B); Pamilican Island, Philippines (site 33A); Huon Peninsula, Papua New Guinea (sites 34A and B), Ryukyu Islands, Japan (site 35), and East Timor (site 36). Given the more limited distribution of MIS 5c data, the restricted dataset for this substage included the above sites with MIS 5c markers—namely sites 3, 15, 18, 29, 30A and B, 33A, 34A and B, 35 and 36—as well as Berry Island, Bahamas (site 28C).

### 3. Methods

Modern geophysical predictions of ice-age sea-level changes date to the pioneering theory of Farrell and Clark (1976), which included viscoelastic deformation of the solid Earth and gravitationally self-consistent redistribution of meltwater, but assumed no lateral shoreline migration—that is, vertical cliffs delineated all shorelines—on a non-rotating Earth. Mitrovica and Milne (2003) extended this earlier theory to allow for shoreline migration due either to local sea-level fluctuations at shorelines or changes in the extent of grounded, marine-based ice cover. Following Milne and Mitrovica (1996, 1998) and Mitrovica et al. (2005), Kendall et al. (2005) incorporated the feedback into sea level of changes in the Earth's rotation into this generalized theory.

We adopt the pseudo-spectral algorithm described by Kendall et al. (2005) using a truncation at spherical harmonic degree and order 256. Our calculations are based on a spherically symmetric (i.e., depth-varying but laterally homogeneous), self-gravitating, Maxwell viscoelastic Earth, with the elastic and density structure of the Earth model given by the seismically inferred model PREM (Dziewonski and Anderson, 1981). The viscosity structure is defined by an elastic lithosphere of prescribed thickness, LT, and uniform upper and lower mantle viscosities denoted by  $\nu_{UM}$  and  $\nu_{LM}$ , respectively.

We construct an ice history over two successive glacial cycles in a manner similar to that described by Muhs et al. (2012). Our ice history is based on a revised version (Austermann et al., 2013) of the ICE-5G model (Peltier, 2004) from LGM to present but differs from ICE-5G (Version 1.2) across an interval spanning the inception of the glaciation phase, beginning at  $\sim 120$  ka, to the LGM. Version 1.2 of ICE-5G assumes that the perimeter of the pre-LGM ice sheets remained fixed at their LGM extent such that variations in ice volume through this interval require a simple scaling of the elevation of LGM ice sheets without change in their areal extent. In our revised ice history, we track the same eustatic change after MIS 5a as adopted by ICE-5G (Version 1.2), but we apply incremental changes in the distribution of the ice load by assuming that, at any time during this glaciation phase, the geometry of ice sheets matched that of the deglaciation phase when eustatic values are equivalent. Finally, we construct a penultimate glacial cycle by duplicating the last glacial cycle and shifting it back in time so that it ends at 131 ka.

Our ice history deviates from the ICE-5G eustatic history between 120 ka and 70 ka by treating eustatic values for MIS 5a ( $\sim 80$  ka), 5b ( $\sim 90$  ka), 5c ( $\sim 100$  ka), and 5d ( $\sim 110$  ka) as free parameters, and varying these values to consider a large number of ice-volume fluctuations (Fig. 1). We have verified that the predictions discussed below are relatively insensitive to the details of the glaciation phase after MIS 5a, as well as to changes of order  $\pm 5$  kyr in the timing of the MIS 5a and 5c high stands. For example, the results do not change significantly if we adopt an age of 85 or 75 ka for peak MIS 5a sea level.

### 4. Results

In the following, we explore predictions of peak relative sea level during MIS 5a and MIS 5c generated by varying the Earth and ice-model parameters discussed above, and assess the fit of each prediction to the available observational constraints. We first consider a small number of representative simulations in order to elucidate the physics that governs the geographic variability in the amplitude of MIS 5a and 5c high stands.

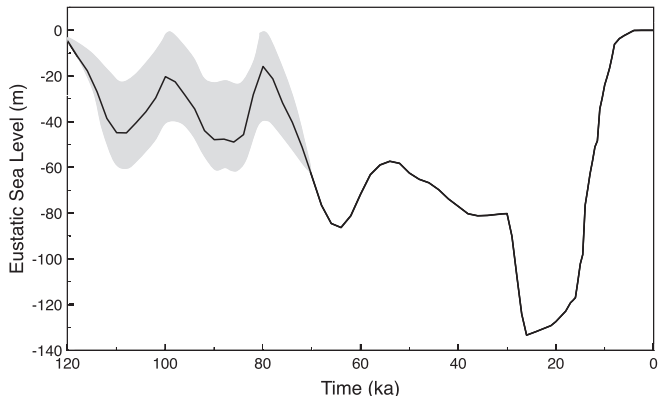


**Fig. 1.** The time history of global mean ('eustatic') sea-level change (solid line) associated with the test ice history adopted in this study. The shaded area from 120 to 70 ka covers the range of eustatic histories extending from MIS 5e to the start of MIS 4 adopted in the sensitivity analysis described in the text.

#### 4.1. Glacial isostatic adjustment: the physics of MIS 5a/5c high stands

GIA-corrected predictions of MIS 5c and MIS 5a high stands have been discussed for the U.S. southeast Atlantic and Caribbean (Potter and Lambeck, 2003), San Nicolas Island, CA (Muhs et al., 2012), and the Pacific Coast extending from Oregon to Baja California Sur, Mexico (Simms et al., 2015). In this section, we extend these GIA predictions to consider the entire globe and provide a physical explanation for the geographic variability seen in these results.

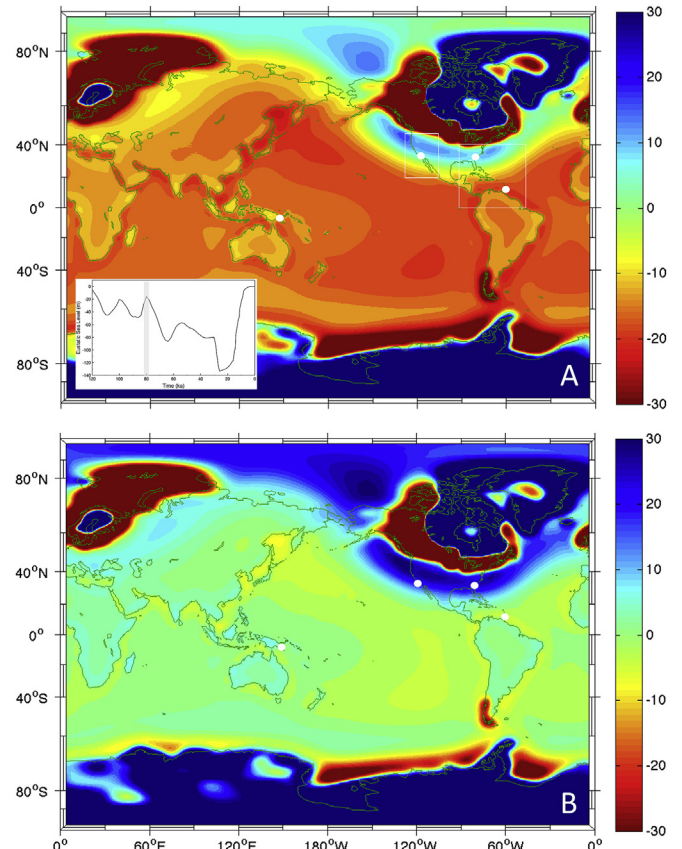
We use an ice history with the equivalent eustatic sea-level history shown by the thick black line in Fig. 1. This history is characterized by peak values of  $-16\text{ m}$  and  $-20\text{ m}$  during MIS 5a and MIS 5c, respectively. In the first simulation, we adopt an Earth model within the range of models preferred by Lambeck et al. (1998) and by Mitrovica and Forte (2004) that is characterized by a lithosphere thickness of  $95\text{ km}$ , upper mantle viscosity  $\nu_{UM} = 5 \times 10^{20}\text{ Pa s}$ , and lower mantle viscosity  $\nu_{LM} = 10^{22}\text{ Pa s}$ .

Fig. 2A shows a global prediction of RSL for MIS 5a at 80 ka. To compare this result with earlier regional predictions, we reproduce the MIS 5a RSL predictions of Potter and Lambeck (2003), who focused on the U.S. Atlantic coastal plain and Caribbean, alongside our prediction for the same area (Fig. 3; the area delineated by the white box in Fig. 2A). Despite differences in the ice history and Earth model, the geometry and amplitude of the two predictions broadly agree, with both showing a strong latitudinal gradient in the predicted high-stand elevation, with elevations decreasing by  $\sim 30\text{ m}$  to the south (Fig. 3). For these Earth-ice model pairings, the Pacific coast of the U.S. and Baja California Sur show the same trend and amplitude in the RSL prediction (Figs. 2A and 4A).

Fig. 2B shows the deviation of the predicted high-stand elevation (Fig. 2A) from the eustatic value adopted in the model run at 80 ka ( $-16\text{ m}$ ; Fig. 1). For most sites in the far field of the LGM ice cover, this deviation is less than  $\sim 3\text{ m}$ , whereas this discrepancy is much larger within the near field and displays a complex geometry.

Fig. 5A shows RSL histories over the last glacial cycle for two sites in the near field (Charleston, SC, and San Nicolas Island, CA) and two sites in the far field (Huon Peninsula, Papua New Guinea and Barbados) of the Laurentide and Cordilleran ice sheets. Whereas the Barbados and Huon Peninsula RSL curves track the eustatic history relatively closely throughout MIS 5, the difference from the eustatic history at the two near-field sites reaches  $\sim 30\text{ m}$  during MIS 5a and MIS 5c.

To explore the origin of these deviations from eustatic, we



**Fig. 2.** (A) Predicted sea level at MIS 5a (80 ka) relative to present day based on the test ice history described in the text, an Earth model characterized by an elastic lithosphere of thickness  $95\text{ km}$ , and upper and lower mantle viscosities of  $5 \times 10^{20}\text{ Pa s}$  and  $10^{22}\text{ Pa s}$ , respectively. The solid line in the inset is the eustatic curve associated with this ice history (reproduced from Fig. 1) and the vertical shading on the inset highlights the high stand that characterizes this ice history. (B) The predicted departure from MIS 5a (80 ka) eustatic sea level derived by subtracting the eustatic value associated with the ice history at 80 ka ( $-15.74\text{ m}$ ) from the relative sea level signal plotted in frame (A). The small white circles on each frame show the location of sites discussed in the text: (from west to east): Huon Peninsula, Papua New Guinea; San Nicolas Island, California; Charleston, South Carolina and Barbados. Outlined boxes over the southeastern U.S. Atlantic coast and Caribbean (right) and Pacific coast of North America (left) are reproduced in Fig. 3B and 4A, respectively.

decompose these predictions into signals from the main contributing processes. The RSL history at a given site ( $\theta, \phi$ ) and time ( $t$ ) can be written as the sum:

$$RSL(\theta, \phi, t) = E(\theta, \phi, t) + GIA(\theta, \phi, t), \quad (1)$$

where the second term on the right-hand side can be decomposed such that:

$$RSL(\theta, \phi, t) = E(\theta, \phi, t) + DG(\theta, \phi, t) + DEF(\theta, \phi, t). \quad (2)$$

In these equations,  $E$  is the eustatic (globally averaged) sea-level history associated with the ice history. The second term on the right-hand side of equation (1) represents the impact of glacial isostatic adjustment (hence the label "GIA") on sea level. In this terminology, Fig. 2A represents RSL at 80 ka, while Fig. 2B shows GIA at 80 ka. In equation (2), the GIA term is decomposed into a contribution from the direct gravitational effect of the surface mass load (DG; so-called self-gravitation of the surface mass load) and a residual term labeled 'DEF'. The latter includes all deformational effects related to isostatic adjustment of the Earth in response to the surface mass load, the gravitational impact of this deformation,

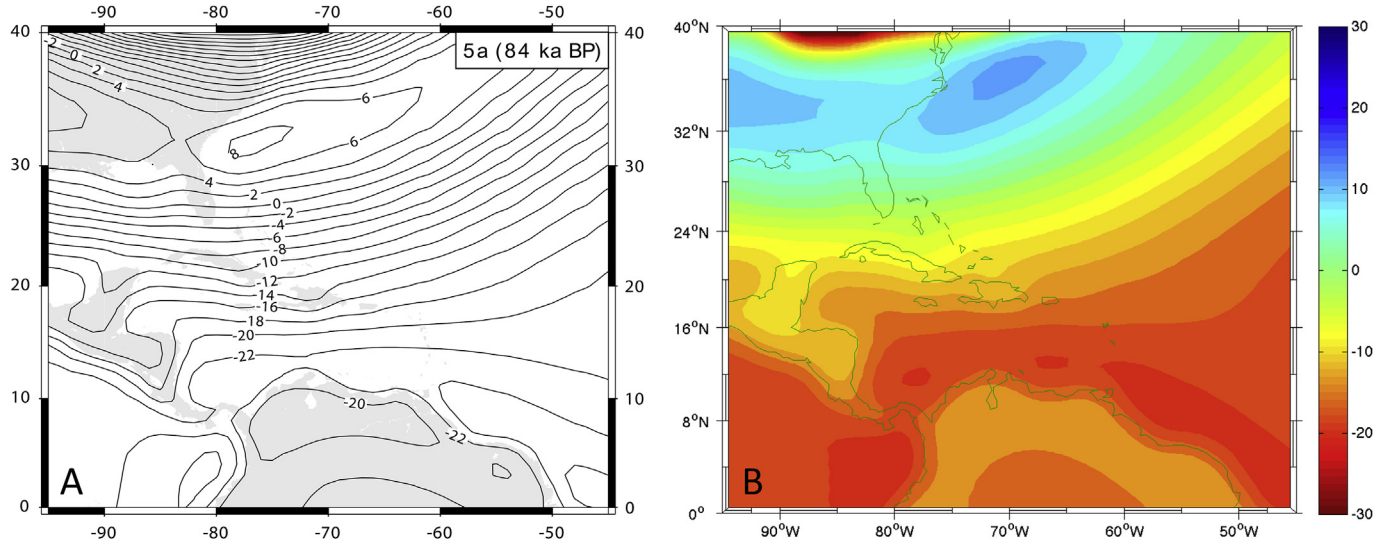


**Fig. 3.** (A) Sea level at 84 ka (MIS 5a) relative to the present day across the western Atlantic between 0°N and 40°N as predicted by Potter and Lambeck (2003). (B) Detail of the relative sea level for MIS 5a (80ka) computed in the present study (reproduced from Fig. 2A) for the region shown in frame (A) and based on the eustatic curve for the ice history shown by the solid line of Fig. 1.

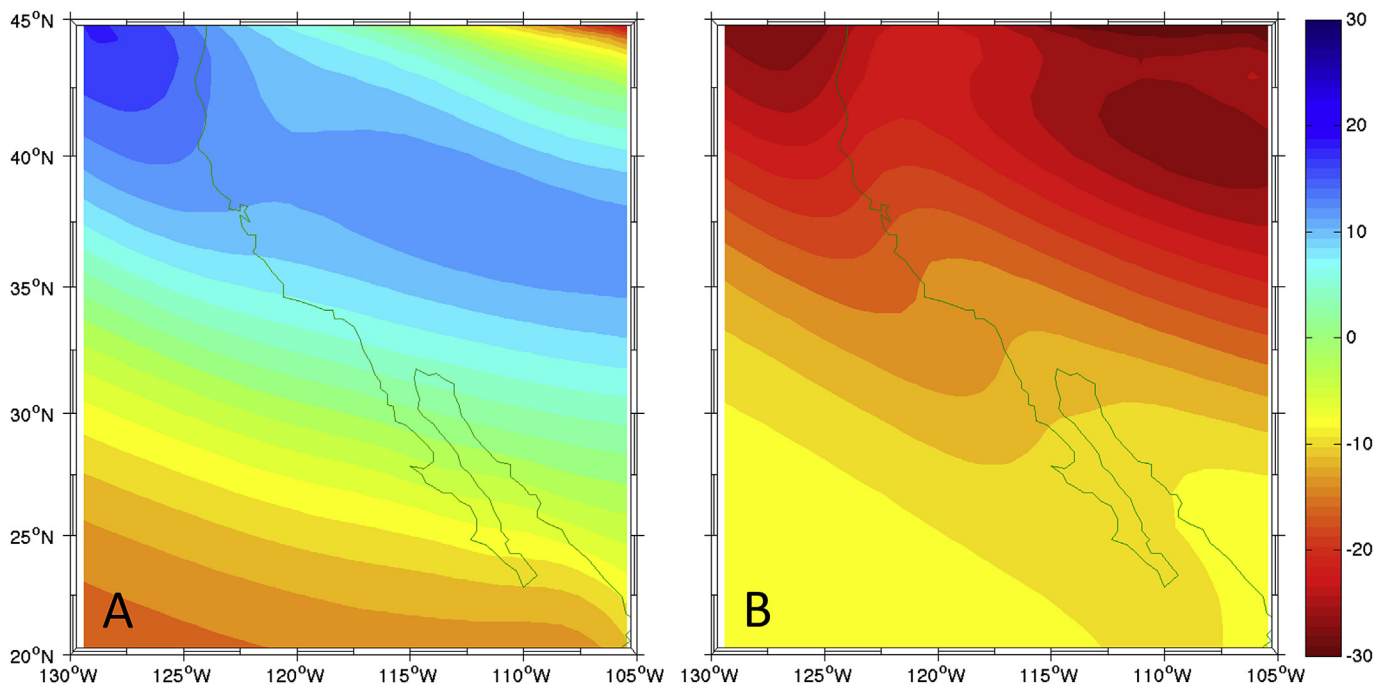


**Fig. 4.** Reproduction of the results of relative sea level for MIS 5a (80 ka) computed in the present study for (A) the scenario shown in Fig. 2A and (B) the scenario shown in Fig. 8A. Both frames show a region that encompasses the Pacific coast of North America from Oregon, U.S.A to Baja California Sur, Mexico.

and the feedback into sea level of perturbations in Earth rotation driven by the changing distribution of ice and water loads (Milne and Mitrovica, 1998).

In Fig. 5B, we decompose the predicted RSL change at Charleston, SC, during the last glacial cycle into the three contributions on the right-hand-side of equation (2). The difference between the predicted RSL and the eustatic curve is 24.6 m during MIS 5a and 27.2 m during MIS 5c. The signals due to deformation and the direct gravitational effect of the surface load are both non-negligible, and of the same sign, through the entire glacial phase, and in particular during MIS 5a and MIS 5c.

**Fig. 6A–C** summarizes the physical processes responsible for these predicted signals. The black dot on the left of each frame represents a near-field site, such as Charleston, SC, or San Nicolas Island, CA, located on the peripheral bulge of the Laurentide and Cordilleran Ice Sheets in the simulation shown in Fig. 2. Fig. 6A shows a situation early in the glacial phase, such as during MIS 5a, when relatively small ice sheets covered North America. From 80 ka to the present, two processes dominated the sea-level change at these near-field sites. First, the elevation of the peripheral bulge generally remained constant or increased through the glaciation phase and then began to subside some time (~5 kyr) after the LGM

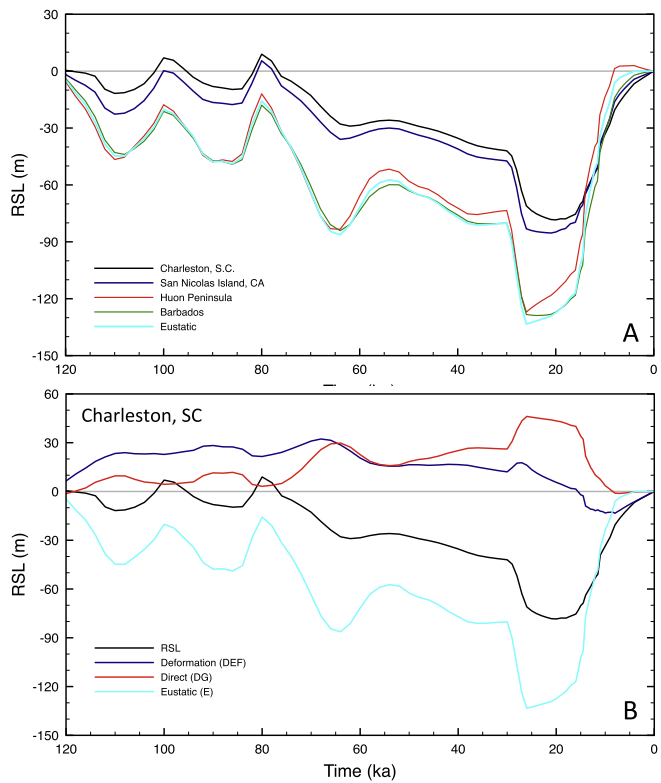


**Fig. 5.** (A) Predicted relative sea level curves for Charleston, South Carolina; San Nicolas Island, California; Huon Peninsula, Papua New Guinea; and Barbados (as labeled) computed using the test ice history and Earth model described in the text. The eustatic curve for the adopted ice history (cyan line) is reproduced from the solid line in Fig. 1. (B) The predicted relative sea level curve at Charleston, South Carolina (solid black line), decomposed into contributions from the eustatic curve (cyan), the direct gravitation effect of the surface mass load (red line) and the deformation signal (blue line; see equation (2) and related text). (For interpretation of the references to colour in this figure legend, the reader is referred to the web version of this article.)

(e.g., see the blue curve of ‘deformation’ in Fig. 5B). At present, the elevation of the bulge is higher than the predicted elevation during MIS 5a, and this difference in crustal elevation contributes to a RSL fall at Charleston or San Nicolas Island (left arrow in Fig. 6B). That is, the level of present-day isostatic disequilibrium at this site on the bulge is greater than the level of disequilibrium early in the glacial phase. Second, the net melting of the Laurentide and Cordilleran ice sheets from 80 ka to present-day reduced the gravitational attraction of the ice sheet onto the ocean and meltwater migrated away from the ice sheet toward the far field, contributing to a drop in near-field sea level (right arrow in Fig. 6B). These two physical processes are incorporated into the DEF and DG terms in equation (2), respectively, and they add constructively so that the GIA prediction for this simulation involves a relatively large sea-level fall at these near-field sites between 80 ka to present day. Finally, the eustatic signal associated with globally integrated melting from 80 ka to present acts in opposition to the predicted GIA signal (Fig. 6C). However, for the simulation in Figs. 2 and 5, the magnitude of this eustatic signal at near-field sites such as Charleston or San Nicolas Island is smaller than the GIA signal and the net effect is a high stand above present-day sea level during MIS 5a (Fig. 5A).

At far-field sites, the direct gravitational effect of the surface-mass load will lead to a sea-level rise from 80 ka to present, as water migrates toward these sites. The predicted magnitude of the DEF term depends on the location of the site. Nevertheless, the total predicted GIA effect at far-field sites during MIS 5a is relatively small and dominated by the eustatic signal (Figs. 2 and 6C).

The predicted GIA trends moving southward from the U.S. Atlantic coastal plain to the Caribbean (Table 1, sites 21–31) and along the Pacific coast of North America (Table 1, sites 1–20) are characterized by a ~30 m decrease in MIS 5a high-stand elevations (Figs. 2, 3B and 4A). The former is consistent with the observational record of Potter and Lambeck (2003; see Table 1). In contrast, the latter is inconsistent with the Simms et al. (2015) compilation from the Pacific coast of North America where, if terrace elevations and age assignments are robust (see Section 2.1), the tectonically

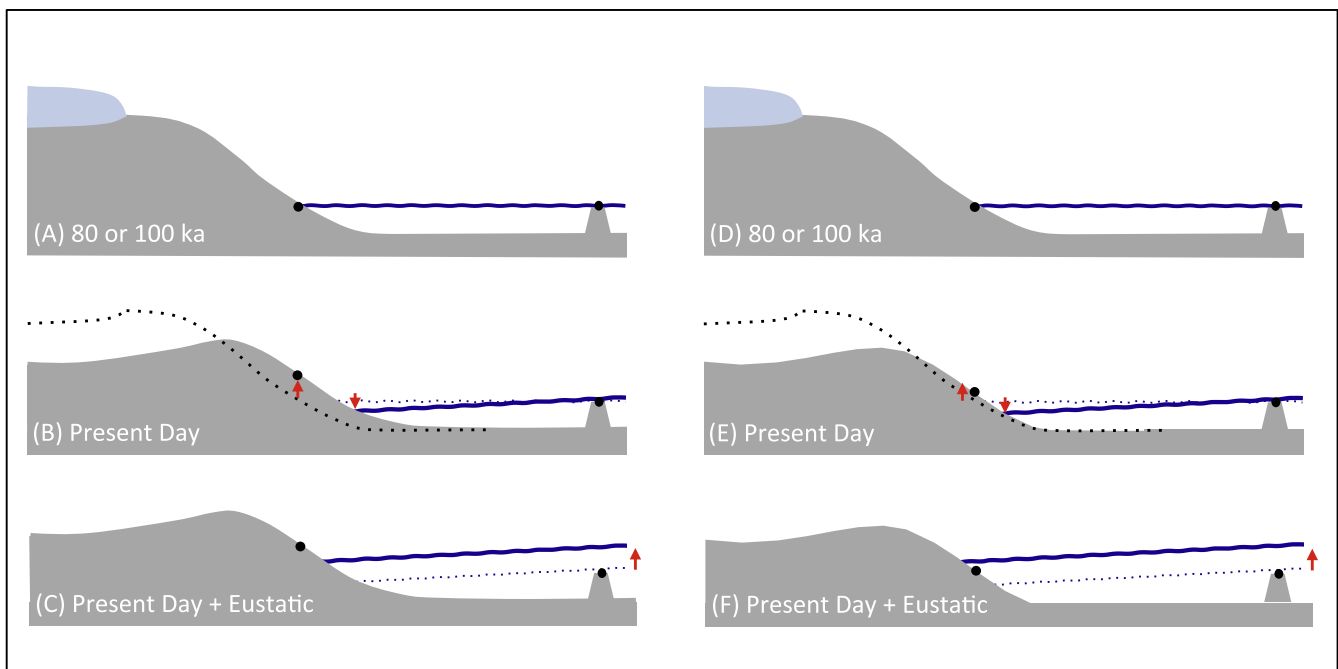


**Fig. 6.** Schematic illustrating the physics of relative sea level during MIS 5a (or, similarly, MIS 5c). Frames (A)–(C) and (D)–(F) illustrate two scenarios distinguished by a difference in the level of peripheral bulge deformation relevant to scenarios illustrated in Fig. 2 and 8, respectively (see text for discussion).

corrected high stands increase by ~20 m as one moves south from northern Oregon to the southern tip of Baja California Sur.

We assess the possibility that the opposing slopes in the reconstructed elevation of peak MIS 5a and 5c high-stand elevations between the Pacific and Atlantic coasts of North America (and the Caribbean) are due to lateral variation in mantle viscosity. In support of this hypothesis, we have not found a GIA prediction, based on a laterally uniform, 1-D viscoelastic Earth model that simultaneously reconciles both trends. To explore this issue further, we estimated viscosity variations within the upper mantle beneath North America from the seismic shear wave velocity model S40RTS (Ritsema et al., 2011) using the method of Austermann et al. (2013) (Fig. 7). While there is uncertainty in the relationship between seismic velocity and viscosity, the geographic trend in upper mantle viscosity is robust and consistent with the differing tectonic settings along the Pacific and Atlantic coasts of North America. The mean upper mantle viscosity along a contour extending from Newport, Oregon, to Los Cabos, Mexico, is a factor of 6 smaller than the value computed along a profile from Virginia to Barbados. We thus repeated the simulation in Fig. 2 using an Earth model where the upper mantle viscosity is reduced from  $5 \times 10^{20}$  Pa s to  $10^{20}$  Pa s (Fig. 8), consistent with the upper bound of an inference from Holocene post-glacial rebound from the northern Cascadia margin (James et al., 2000).

A comparison of Figs. 2 and 8 shows that the greatest differences in the simulations are in the location and amplitude of the peripheral bulge of the Laurentide and Cordilleran ice sheets. The simulation with a weak upper mantle predicts a peripheral bulge situated much further from the former ice sheets (Fig. 8). For instance, the calculation adopting the higher upper mantle viscosity predicts that the peak of the bulge adjustment occurs in North Carolina and Oregon (Fig. 2A; Figs. 3B and 4A), whereas these peaks shift south to the southern tip of Cuba and Baja California Sur when using a weaker upper mantle (Figs. 8 and 4B). Moreover, the peak amplitude of the bulge for the weaker upper mantle scenario is ~8 m (Fig. 8B), versus >30 m in the scenario with a higher upper mantle viscosity (Fig. 2B). Thus, in contrast to the case shown in Fig. 6A–C, where sea-level fall at a near-field site like Charleston—associated with peripheral bulge dynamics and self-gravitation (Fig. 6B)—dominates the eustatic component of the ice history between 80 ka and the present (Fig. 6C), the Earth model

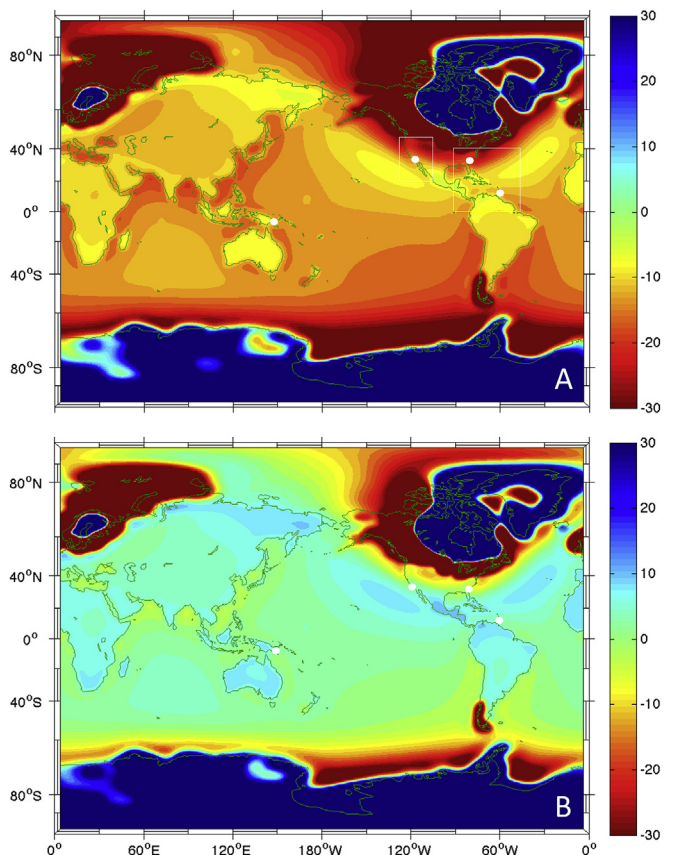


**Fig. 8.** As in Fig. 2, except that the Earth model is characterized by upper and lower mantle viscosities of  $10^{20}$  Pa s and  $5 \times 10^{21}$  Pa s, respectively. Results within the box over the Pacific coast of North America in frame A are reproduced in Fig. 4B.

with a weaker upper mantle (Fig. 8) predicts that the combined effect of peripheral bulge dynamics and self-gravitation is smaller than the eustatic rise. The net result is that the high stands at sites such as Charleston and San Nicolas Island are predicted to be well below present-day sea level (Fig. 8A). The physical mechanisms for this scenario are summarized in Fig. 6D–F.

The simulation adopting a relatively high viscosity upper mantle (Fig. 2) places the east- and west-coasts of North America (south of Canada) on the far-field side (i.e., outer flank) of a significant peripheral bulge, and thus the predicted GIA signal decreases towards the south. This trend is consistent with the east-coast sea-level indicators (Potter and Lambeck, 2003), but it is inconsistent with the west-coast indicators (Simms et al., 2015). In contrast, in the case of a weaker upper mantle region, the same sites are predicted to sit on the near-field side (i.e., inner flank) of a more muted peripheral bulge such that the GIA signal increases toward the south (Fig. 8). This agrees with the west-coast sea-level indicators but not the east-coast indicators (Table 1). These results suggest lateral variations in mantle viscosity consistent with previous studies, where the preferred Earth model used by Potter and Lambeck (2003) had a significantly higher upper mantle viscosity than the one used by Simms et al. (2015). In the following, we thus allow for distinct 1-D Earth models for each geographic region, as well as for the set of remaining far-field sites in Table 1.

#### 4.2. Bounding peak global mean sea level during MIS 5a and 5c

We next turn to a Monte Carlo statistical procedure aimed at

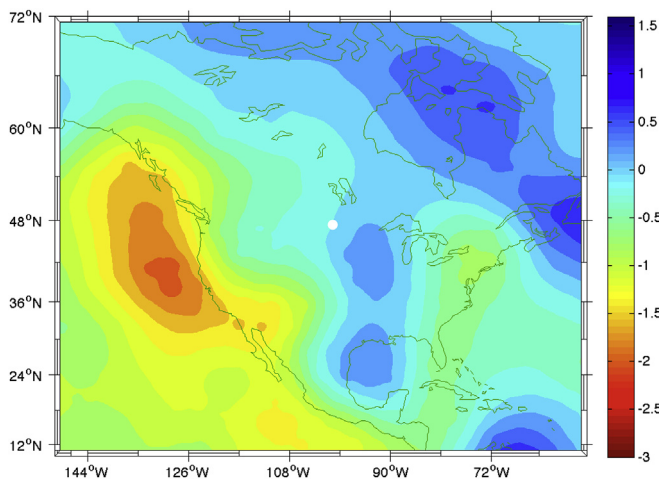


**Fig. 7.** Geographic variation in the volumetric mean upper mantle viscosity in the vicinity of North America. The field is inferred from seismic shear wave tomography model S40RTS (Ritsema et al., 2011) following the multi-step method described in Austermann et al. (2013). Contours show the logarithm of the viscosity relative to the value at a site shown by the white dot at the center of the continent.

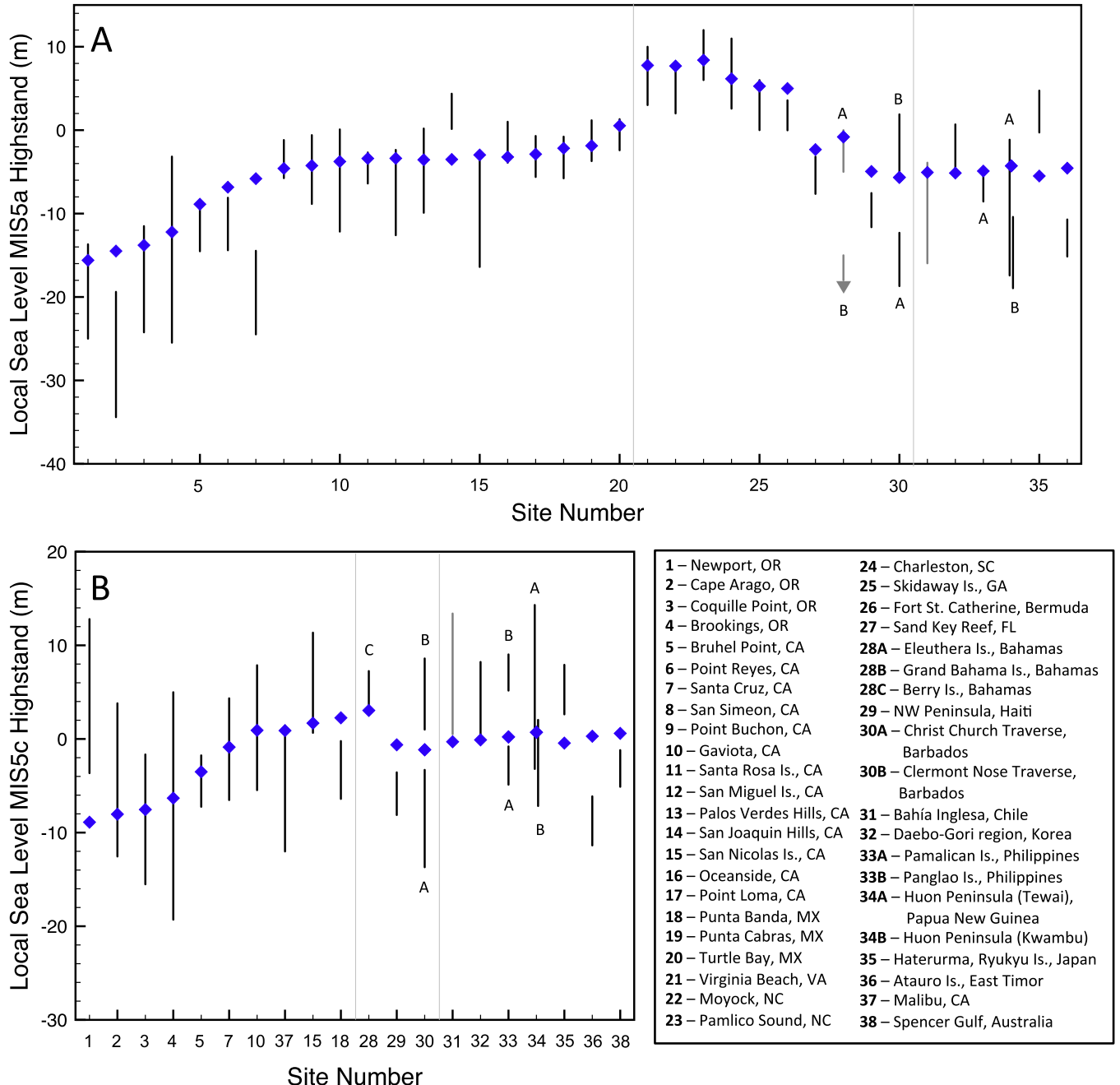


**Fig. 9.** Predictions of high stand elevations (blue diamonds) for a series of sites (see legend) during (A) MIS 5a and (B) MIS 5c based on the ice-age sea level simulation that best fits geological observations (Table 1) after correction for tectonic effects (black vertical bars; errors in Table 1 have been augmented to incorporate uncertainties in the tectonic correction following Creveling et al., 2015). The observational records for Eleuthera and Grand Bahamas Is. (sites 28A and 28B) and Bahía Inglesa, Chile (31) are shown as gray lines because these data are not used within the Monte Carlo analysis establishing the best-fit GIA simulation and the bounds on peak GMSL during MIS 5a and 5c (see text). The two solid light gray vertical lines within each frame separate sites along the Pacific coast of the United States and Mexico (left), the U.S. Atlantic coastal plain to the Caribbean (middle), and the far-field of late Pleistocene ice sheets (right). (For interpretation of the references to colour in this figure legend, the reader is referred to the web version of this article.)

bounding coeval peak GMSL. To this end, we performed a large series of GIA simulations in which we adopted 200 unique eustatic sea-level histories for the last glacial cycle that sampled the bounds shown in Fig. 1. We also chose a set of Earth models sampling upper ( $v_{UM}$ ) and lower ( $v_{LM}$ ) mantle viscosity values in the range  $0.8\text{--}5 \times 10^{20}$  Pa s and  $4\text{--}30 \times 10^{21}$  Pa s, respectively. In each simulation we followed a standardized procedure:

- Step 1: Predict peak GIA-induced high stands during MIS 5a and MIS 5c for all sites in Table 1;
- Step 2: Predict GIA-induced relative sea level across MIS 5e for each site (Table 1) assuming that ice volume, and thus eustatic sea level, during this period was identical to the present;
- Step 3: Add to the MIS 5e GIA signal (step 2) an excess melt signal computed from an interglacial ice-sheet collapse scenario with a eustatic rise ranging from 6 to 8 m (Kopp et al., 2009; Dutton and Lambeck, 2012; Hay et al., 2014);

Step 4: Subtract the peak MIS 5e high-stand amplitudes computed in step (3) from the observed MIS 5e high stands ([Table 1](#)), and use the residuals to estimate the tectonic uplift/subsidence rate for all sites (following the method outlined by [Creveling et al., 2015](#)); for field sites without a local MIS 5e high stand, we apply the tectonic rates adopted in the original publication of the data (for many sites, including those along the U.S. east coast, an assumption of tectonic stability yields a nominal correction);

Step 5: Correct observed MIS 5a and 5c high stands at all sites ([Table 1](#)) for tectonic deformation using the rates computed in step (4);

Step 6: Compare the high-stand amplitudes during MIS 5a and MIS 5c obtained in step (5) with numerically predicted high stands from step (1), and compute the total misfit for three regional bins: sites along the Pacific coast of North America, sites along the east coast of North America and the Caribbean, and all other sites in [Table 1](#);

Step 7: Repeat steps (3)–(6) for the suite of different ice-sheet collapse scenarios during MIS 5e that sample the full eustatic range (6–8 m), considering different relative contributions from the Greenland Ice Sheet, Antarctic Ice Sheet, and mountain glacier melt, and adopting different timings for the excess melt signal (early or late in the MIS 5e period; see [Creveling et al., 2015](#));

Step 8: Repeat steps (1)–(7) for all Earth models;

Step 9: Repeat steps (1)–(8) for all ice histories ([Fig. 1](#)).

This exercise yields a large set of misfits, each paired with an input peak GMSL (eustatic) value for both the MIS 5a and MIS 5c high stands.

We describe below the results of two separate analyses in which: (1) we use the full database summarized in [Table 1](#), with a few exceptions related to sites with multiple, but discordant records; and (2) we repeat the steps above with a smaller set of sites characterized by particularly robust temporal constraints on MIS 5 paleo-shoreline makers.

[Fig. 9](#) shows the forward GIA prediction of MIS 5a and MIS 5c high stands with the smallest global  $\chi^2$  residual (blue diamonds) compared to the observed range for high-stand elevations after correction for tectonic deformation (vertical bars). This analysis includes all sites in [Table 1](#) except the records from Bahamas (Eleuthera and Grand Bahamas) and Bahía Ingresa, Chile (dark gray vertical bars), which are not included in the calculation of misfit. This best-fitting GIA simulation is characterized by a GMSL during MIS 5a and 5c of  $-6.2$  m and  $-1.7$  m, respectively, and upper and lower mantle viscosity pairs of  $(0.1 \times 10^{21}, 5 \times 10^{21} \text{ Pa s})$ ,  $(0.5 \times 10^{21}, 4 \times 10^{21} \text{ Pa s})$  and  $(0.5 \times 10^{21}, 2.8 \times 10^{21} \text{ Pa s})$ , for sites on the Pacific coast of North America, the U.S. east coast south to the Caribbean, and the far field, respectively.

The best-fit GIA prediction is in good agreement with the geographic trends in high-stand elevation along the Pacific coast of North America (where high stands increase in elevation toward the south) and the east coast of the U.S. south through the Caribbean (where they tend to decrease toward the south). The misfits, where they exist, motivate a re-evaluation of the observational data and, more likely, the tectonic and/or growth- or depositional-depth corrections applied to the indicators, since the corrected records from these sites do not appear to follow the general geographic trend of the adjacent (corrected) high-stand indicators.

In the case of the Pacific coast of North America for MIS 5a ([Fig. 9A](#)), the corrected observational data from Cape Arago and Santa Cruz fall below numerical predictions (in contrast, the MIS 5c high stand observations are compatible with the predictions at these sites), while the San Joaquin Hills datum falls above

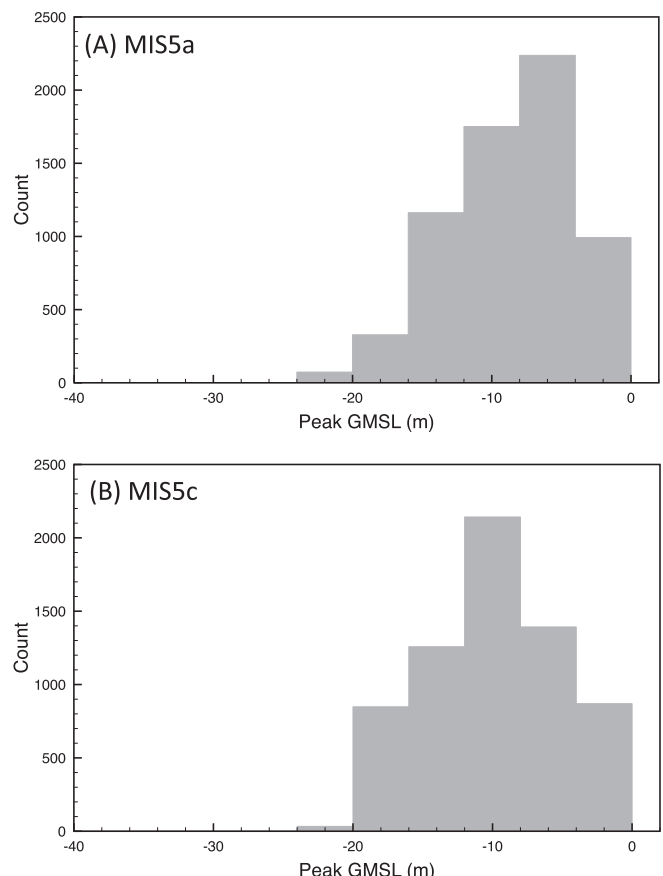


**Fig. 10.** Histograms of peak GMSL values during (A) MIS 5a and (B) MIS 5c for a subset of ice-age sea level simulations chosen on the basis of minimized misfit between the predicted and observed (after tectonic correction) high stand elevations (see text).

numerical predictions. The misfit of the MIS 5a record at Santa Cruz may reflect problems with the age assignment ([Muhs et al., 2006](#)). Indeed, [Simms et al. \(2015\)](#) discussed alternative terrace age assignments that would reconcile the high-stand record at Santa Cruz with the numerical prediction. Misfits in MIS 5c high stands along the Pacific coast are associated with Newport, OR, and Punta Banda ([Fig. 9B](#)), although these are not large relative to the uncertainty in the corrected observations at these sites.

Although the Bahamas records were not included in the calculation of misfit to the MIS 5a records, the best-fit GIA solution is consistent with the peak MIS 5a high stand inferred by [Hearty and Kaufman \(2000\)](#). In contrast, this solution falls well above the upper bound high-stand elevation implied by the speleothem record of [Richards et al. \(1994\)](#). In regard to the Barbados record, the best-fit GIA solution falls between the peak MIS 5a and MIS 5c high stands inferred from the Christ Church and Clermont Nose traverses (although the prediction for MIS 5a skirts the lower bound of the observational constraint at the latter site). The high stand predictions for MIS 5a and 5c at Haiti misfit the observational constraints by a comparable,  $\sim 2$  m margin, and this may suggest a small error in the tectonic correction.

The best-fit GIA solution yields sea level predictions at far-field sites that are  $\sim 4$  m below present for MIS 5a and at present level for MIS 5c; these predictions fall in the mid range of the tectonically corrected high-stand elevations at these sites. We note that the predicted peak high stands during MIS 5a and 5c lie below the associated observations at Ryukyu Island, Japan, and above the observations at the site in East Timor, also suggesting the possibility

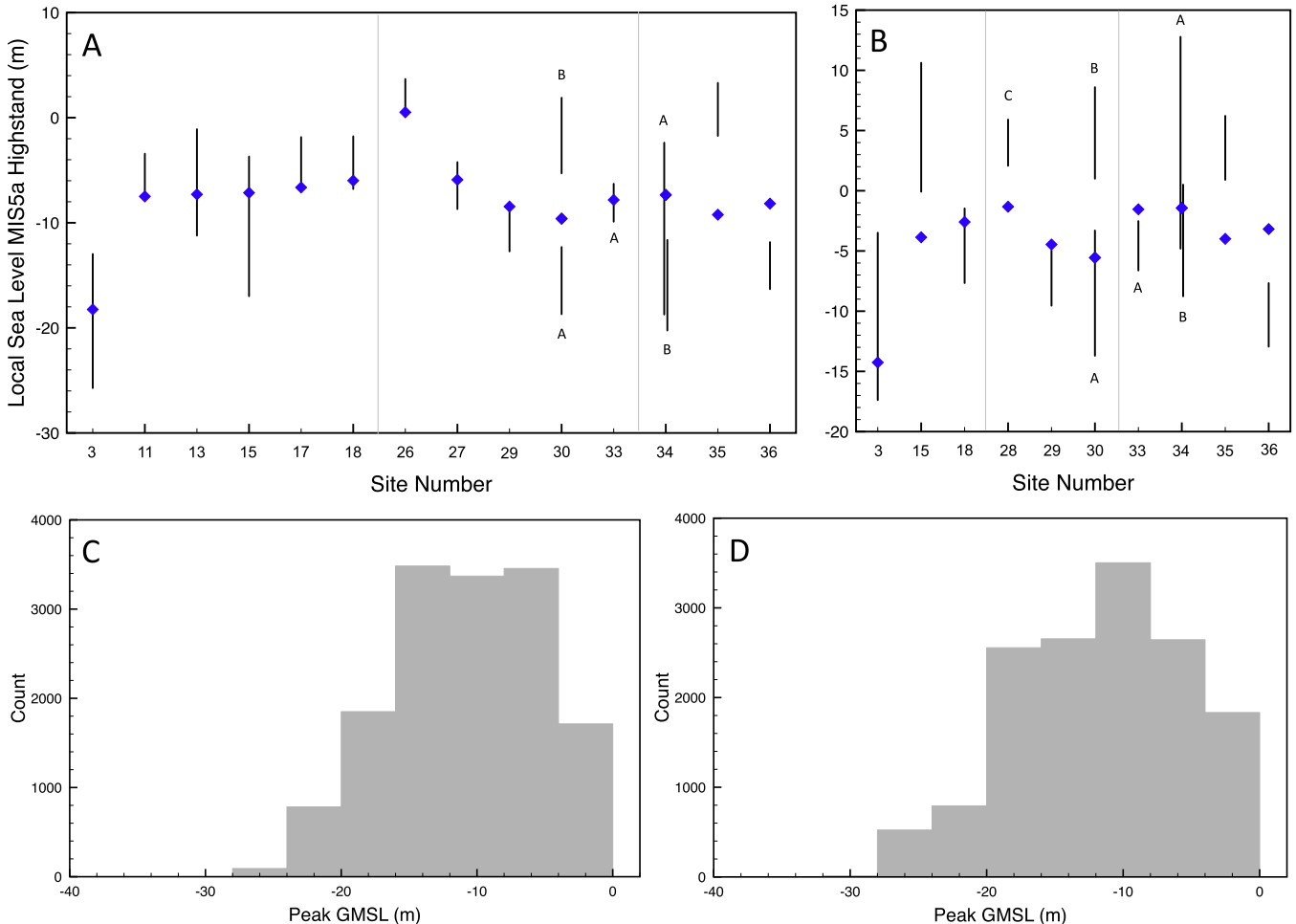


**Fig. 11.** Predictions of high stand elevations (blue diamonds) for a series of sites during (A) MIS 5a and (B) MIS 5c based on the ice-age sea level simulation that best fits a particularly robust subset of geological observations (see text) after these observations have been corrected for tectonic effects (vertical bars). Numbers on the abscissa refer to sites listed in the legend on Fig. 9. The two light gray vertical lines within each frame separate sites along the Pacific coast of the United States and Mexico (left), the U.S. Atlantic coastal plain to the Caribbean (middle), and the far-field of late Pleistocene ice sheets (right). Histograms of peak GMSL values during (C) MIS 5a and (D) MIS 5c for a subset of ice-age sea level simulations chosen on the basis of minimized misfit between the predicted and observed (after tectonic correction) high stand elevations at sites in frames A and B (see text). (For interpretation of the references to colour in this figure legend, the reader is referred to the web version of this article.)

of an error in the tectonic correction applied at these sites.

To derive a preferred range for the peak GMSL during MIS 5a and MIS 5c, we applied an F-test to identify the subset of simulations with a  $\chi^2$  residual that was not significantly different, at 90% confidence, from the minimum  $\chi^2$  residual of all simulations (i.e., the  $\chi^2$  residual of the solution plotted as blue dots in Fig. 9). Fig. 10 shows histograms of the range of peak GMSL that characterize this subset of simulations during MIS 5a and MIS 5c. These results indicate that peak GMSL reached  $-18$  m to  $+1$  m relative to present level (mean of  $-8.5 \pm 4.6$  m,  $1\sigma$  range; quartiles of  $-11.5$  m,  $-7.5$  m,  $-5.9$  m) during MIS 5a and  $-20$  m to  $+1$  m during MIS 5c ( $-9.4 \pm 5.3$  m;  $-13.0$  m,  $-9.1$  m,  $-5.7$  m). These bounds provide tighter constraints on estimates of peak GMSL than those derived from marine  $\delta^{18}\text{O}$  records that, in the case of MIS 5a, vary from  $-40$  m to over  $10$  m (e.g., Shackleton, 2000; Siddall et al., 2003). Furthermore, they rule out some previous estimates based on regional subsets of the sea-level database considered here. For example, from their analysis of high-stand records on the U.S. Atlantic coastal plain and in the Caribbean, Potter and Lambeck (2003) concluded that GMSL during both MIS 5a and MIS 5c peaked at  $\sim 28$  m below present, well below our inferred range. In contrast, estimates from the Pacific coast, the Florida Keys and

Barbados (Muhs et al., 2012; Simms et al., 2015) fall within the bounds suggested by Fig. 10.

To assess the impact of the uncertainty in the age constraints for MIS 5 sea-level indicators, we repeated the Monte Carlo analysis with a subset of records characterized by particularly robust age control and a well-defined relationship to former sea level (Table 1, Fig. 11). The peak GMSL values for MIS 5a and 5c associated with the best-fit GIA solution are  $-9.9$  m and  $-5.8$  m, respectively. The more restrictive set of sites adopted in this analysis yields broader and more uniform histograms (relative to Fig. 10) of preferred peak GMSL values during MIS 5a and 5c. These histograms (Fig. 11C and D) suggest bounds on peak GMSL of  $-22$  m to  $+1$  m (mean of  $-10.5 \pm 5.5$  m; quartiles of  $-14.1$  m,  $-10.4$  m,  $-6.4$  m) and  $-24$  m to  $+2$  m ( $-11.1 \pm 6.6$  m;  $-17.0$  m,  $-10.2$  m,  $-5.8$  m) relative to present levels, respectively.

Since the more restrictive analysis presented in Fig. 11A includes only a single site north of the central coast of California (Coquille Point, OR), the robustness of the north-south trend evident in the North American Pacific coast records reported by Simms et al. (2015), and reproduced in Fig. 9A, is weakened. Nevertheless, for the class of GIA models considered here, the gradient in high-stand elevations between Coquille Point and sites in California and

Mexico in Fig. 11A, like the more distinctive trend evident in Fig. 9A (sites 1–20), is best reconciled by an Earth model with a weaker upper mantle for west coast sites (a viscosity of  $\sim 10^{20}$  Pa s or less) relative to east coast sites. This analysis based on fewer, but better dated, sites thus supports the conclusion that lateral variation in mantle structure plays an important role in geographic trends in high stand elevations and consequent inferences of peak sea level during MIS 5.

## 5. Conclusions

We have presented a suite of predictions of RSL during MIS 5a and 5c based on a theory of post-glacial sea-level change that incorporates the deformational, gravitational, and rotational signals associated with GIA. Through these analyses, we identified the global-scale physics controlling local peak sea level through MIS 5a and 5c (Figs. 2–8). In the far field of late-Pleistocene ice cover, the relative sea-level signal is dominated by eustasy, with additional contributions from deformation induced by ocean loading, rotational effects, and a gravitationally driven migration of water away from near field regions. In the near field, notably along the Pacific and Atlantic coasts of North America, and south through the Caribbean, RSL during MIS 5a and 5c reflects a combination of eustasy, peripheral bulge dynamics, and gravitational effects.

A comparison of our predictions with an unfiltered database of peak high stands indicates that the Pacific coast of North America, extending from Oregon to Baja California Sur, lies on the inner flank of the peripheral bulge of the Laurentide–Cordilleran Ice Sheets, whereas the area from the mid-Atlantic coast of the U.S. to the Caribbean sits on the outer flank of this bulge. From the perspective of GIA physics, this difference can be reconciled by imposing a weaker upper mantle beneath western North America relative to the eastern U.S. and Caribbean, which tends to move the bulge outward from the center of glaciation. Seismic tomographic imaging of upper mantle structure beneath the continent supports this explanation and a future analysis using models of GIA that incorporate 3-D Earth structure (e.g., Latychev et al., 2005) is warranted.

We have also provided refined and statistically robust bounds on peak GMSL during MIS 5a and 5c. To this end, we performed a sensitivity analysis in which we computed GIA predictions for a wide range of GMSL histories and a set of Earth models using a rigorous, self-consistent approach to correct for tectonic deformation. Using all sites in the compiled database, we conclude that peak GMSL reached  $-18$  m to  $+1$  m during MIS 5a and  $-20$  m to  $+1$  m during MIS 5c relative to present sea level. These ranges are broadened to  $-22$  m to  $+1$  m and  $-24$  m to  $+2$  m when using only the best-dated high stand records. Within this predicted range, the lowest values overlap previously published  $2\sigma$  upper bounds on MIS 5 peak GMSL sea level derived from conversions of benthic and planktic  $\delta^{18}\text{O}_{\text{Carb}}$  records (see, for instance, Waelbroeck et al., 2002; Shakun et al., 2015). Our analysis suggests, however, that MIS 5a and/or 5c sea level may have peaked higher than previously estimated, to within a few meters of present sea level. If MIS 5a or 5c GMSL reached these levels, then the scaling between globally distributed, GIA-corrected paleo-sea level markers and  $\delta^{18}\text{O}_{\text{Carb}}$ -derived estimates should be revisited.

## Acknowledgments

This research was supported in part by a donation from the G. Unger Vetlesen Foundation to Oregon State University (J.R.C.), Harvard University (J.X.M.), and NSF grants 1335197 and 1503032 (P.U.C.). We thank Daniel R. Muhs and an anonymous reviewer for thorough and insightful comments that strengthened this submission.

## References

- Adams, J., 1984. Active deformation of the Pacific Northwest continental margin. *Tectonics* 3, 449–472. <http://dx.doi.org/10.1029/TC003i004p00449>.
- Addicott, W.O., Emerson, W.K., 1959. Late pleistocene invertebrates from Punta Cabras, Baja California, Mexico. *Am. Mus. Novitates* 1925, 1–33.
- Anderson, R.S., Menking, K.M., 1994. The Quaternary marine terraces of Santa Cruz, California: evidence for coseismic uplift on two faults. *Geol. Soc. Am. Bull.* 106, 649–664.
- Austermann, J., Mitrovica, J.X., Latychev, K., Milne, G.A., 2013. Barbados-based estimate of ice volume at Last Glacial Maximum affected by subducted plate. *Nat. Geosci.* 6, 553–557.
- Bard, E., Hamelin, B., Fairbanks, R.G., 1990. U-Th ages obtained by mass spectrometry in corals from Barbados: sea level during the past 130,000 years. *Nature* 346, 456–458.
- Bender, M.L., Fairbanks, R.G., Taylor, F.W., Matthews, R.K., Goddard, J.G., Broecker, W.S., 1979. Uranium-series dating of the pleistocene reef tracts of Barbados, West Indies. *Geol. Soc. Am. Bull.* 90 (6), 577–594.
- Berger, G.W., Hanson, K.L., 1992. Thermoluminescence ages of estuarine deposits associated with Quaternary marine terraces, south-central California. In: Fletcher, C.H., Wehmiller, J. (Eds.), *Quaternary Coasts of the United States: Marine and Lacustrine Systems*. Society for Sedimentary Geology Special Publication 48, pp. 303–308.
- Birkeland, P.W., 1972. Late quaternary eustatic sea-level changes along the Malibu coast, Los Angeles county, California. *J. Geol.* 80, 432–448. <http://dx.doi.org/10.1086/627765>.
- Bloom, A.L., Broecker, W.S., Chappell, J.M.A., Matthews, R.K., Mesolella, K.J., 1974. Quaternary sea level fluctuations on a tectonic coast: new  $230\text{Th}234\text{U}$  dates from the Huon Peninsula, New Guinea. *Quat. Res.* 4, 185–205.
- Broecker, W.S., Thurber, D.L., Goddard, J., Ku, T.L., Matthews, R.K., Mesolella, K.J., 1968. Milankovitch hypothesis supported by precise dating of coral reefs and deep-sea sediments. *Science* 159, 297–300.
- Chappell, J., 1974. Geology of coral terraces, Huon Peninsula, New Guinea: a study of Quaternary tectonic movements and sea-level changes. *Geol. Soc. Am. Bull.* 85, 553–570.
- Chappell, J., Shackleton, N.J., 1986. Oxygen isotopes and sea level. *Nature* 324, 137–140.
- Chappell, J., Veeh, H.H., 1978. Late quaternary tectonic movements and sea-level changes at Timor and Atauro island. *Geol. Soc. Am. Bull.* 89 (3), 356–368.
- Chen, J.L., Wilson, C.R., Tapley, B.D., 2013. Contribution of ice sheet and mountain glacier melt to recent sea level rise. *Nat. Geosci.* 6, 549–552. <http://dx.doi.org/10.1038/NGEO1829>.
- Choi, S.-J., Merritts, D.J., Ota, Y., 2008. Elevations and ages of marine terraces and late Quaternary rock uplift in southeastern Korea. *J. Geophys. Res.* 113 (B10403) <http://dx.doi.org/10.1029/2007JB005260>.
- Clarke, G.K.C., Marshall, S.J., 2002. Isotopic balance of the Greenland Ice Sheet: modelled concentrations of water isotopes from 30,000 BP to present. *Quat. Sci. Rev.* 21, 419–430.
- Coyne, M.K., Jones, B., Ford, D., 2007. Highstands during marine isotope stage 5: evidence from the ironshore formation of Grand Cayman, British West Indies. *Quat. Sci. Rev.* 26, 536–559.
- Creveling, J.R., Mitrovica, J.X., Hay, C.C., Austermann, J., Kopp, R.E., 2015. Revisiting tectonic corrections applied to Pleistocene sea-level highstands. *Quat. Sci. Rev.* 111, 72–80.
- Cronin, T.M., Szabo, B.J., Ager, T.A., Hazel, J.E., Owens, J.P., 1981. Quaternary climates and sea levels of the US Atlantic coastal plain. *Science* 211, 233–240.
- Cutler, K.B., Edwards, R.L., Taylor, F.W., Cheng, H., Adkins, J., Gallup, C.D., Cutler, P.M., Burr, G.S., Bloom, A.L., 2003. Rapid sea-level fall and deep-ocean temperature change since the last interglacial period. *Earth Planet. Sci. Lett.* 206, 253–271.
- Dalca, A.V., Ferrier, K.L., Mitrovica, J.X., Perron, J.T., Milne, G.A., Creveling, J.R., 2013. On postglacial sea level—III. Incorporating sediment redistribution. *Geophys. J. Int.* 194, 45–60.
- Dodge, R.E., Fairbanks, R.G., Benninger, L.K., Maurrasse, F., 1983. Pleistocene sea levels from raised coral reefs of Haiti. *Science* 219, 1423–1425.
- Dumas, B., Hoang, C.T., Raffy, J., 2006. Record of MIS 5 sea-level highstands based on U/Th dated coral terraces of Haiti. *Quat. Int.* 145, 106–118.
- Dutton, A., Lambeck, K., 2012. Ice volume and sea level during the Last Interglacial. *Science* 337, 216–219.
- Dutton, A., Carlson, A.E., Long, A.J., Milne, G.A., Clark, P.U., DeConto, R., Horton, B.P., Rahmstorf, S., Raymo, M.E., 2015. Sea-level rise due to polar ice-sheet mass loss during past warm periods. *Science* 349. <http://dx.doi.org/10.1126/science.aaa4019>.
- Dziewonski, A.M., Anderson, D.L., 1981. Preliminary reference Earth model (PREM). *Phys. Earth Planet. Int.* 25, 297–356.
- Edwards, R.L., Cheng, H., Murrell, M.T., Goldstein, S.J., 1997. Protactinium-231 dating of carbonates by thermal ionization mass spectrometry: implications for Quaternary climate change. *Science* 276, 782–786.
- Elderfield, H., Greaves, M., Barker, S., Hall, I.R., Tripathi, A., Ferretti, P., Crowhurst, S., Booth, L., Daunt, C., 2010. A record of bottom water temperature and seawater  $\delta^{18}\text{O}$  for the Southern Ocean over the past 440 kyr based on Mg/Ca of benthic foraminiferal *Uvigerina* spp. *Quat. Sci. Rev.* 29, 160–169.
- Emerson, W.K., Kennedy, G.L., Wehmiller, J.F., Keenan, E., 1981. Age relations and zoogeographic implications of late Pleistocene marine invertebrate faunas from Turtle Bay, Baja California Sur, Mexico. *Natur.* 95, 105–116.

- Esat, T.M., McCulloch, M.T., Chappell, J., Pillans, B., Omura, A., 1999. Rapid fluctuations in sea level recorded at Huon Peninsula during the penultimate deglaciation. *Science* 283, 197–201.
- Farrell, W.E., Clark, J.A., 1976. On postglacial sea level. *Geophys. J. R. Astr. Soc.* 46, 647–667.
- Focke, J.W., 1978. Limestone cliff morphology on Curaçao (Netherlands Antilles), with special attention to the origin of notches and vermetid/coralline algal surf benches ("cornices", "trottoirs"). *Z. für Geomorphol.* 22, 329–349.
- Gallup, C.D., Cheng, H., Taylor, F.W., Edwards, R.L., 2002. Direct determination of the timing of sea level change during Termination II. *Science* 295, 310–313.
- Goreau, T.F., 1959. The ecology of Jamaican coral reefs. I. Species composition and zonation. *Ecology* 40, 67–90.
- Grant, L.B., Mueller, K.J., Gath, E.M., Cheng, H., Edwards, R.L., Munro, R., Kennedy, G.L., 1999. Late Quaternary uplift and earthquake potential of the San Joaquin Hills, southern Los Angeles basin, California. *Geology* 27, 1031–1034. [http://dx.doi.org/10.1130/0091-7613\(1999\)027<1031:LQUAEP>2.3.CO;2](http://dx.doi.org/10.1130/0091-7613(1999)027<1031:LQUAEP>2.3.CO;2).
- Grove, K., Sklar, L.S., Scherer, R., Lee, G., Davis, J., 2010. Accelerating and spatially-varying crustal uplift and its geomorphic expression, San Andreas fault zone north of San Francisco, California. *Tectonophysics* 495, 256–268. <http://dx.doi.org/10.1016/j.tecto.2010.09.034>.
- Hails, J.R., Belcher, A.P., Gostin, V.A., Sargent, G.E.G., 1984. The submarine Quaternary stratigraphy of northern Spencer Gulf, South Australia. *Mar. Geol.* 61, 345–372.
- Hanson, K.L., Lettis, W.R., Wesling, J.R., Kelson, K.I., Mezger, L., 1992. Quaternary marine terraces, south-central coastal California: implications for crustal deformation and coastal evolution. In: Fletcher, C.H., Wehmiller, J.F. (Eds.), *Quaternary Coasts of the United States: Marine and Lacustrine Systems*. Society for Sedimentary Geology Special Publication 48, pp. 323–332.
- Harmon, R.S., Mitterer, R.M., Kriausakul, N., Land, L.S., Schwarzc, H.P., Garrett, P., Larson, G.J., Vacher, H.L., Rowe, M., 1983. U-series and amino-acid racemization geochronology of Bermuda: implications for eustatic sea-level fluctuation over the past 250,000 years. *Palaeogeogr. Palaeoclimatol. Palaeoecol.* 44 (1), 41–70.
- Hay, C., Mitrovica, J.X., Gomez, N., Creveling, J.R., Austermann, J., Kopp, R.E., 2014. The sea-level fingerprints of ice-sheet collapse during interglacial periods. *Quat. Sci. Rev.* 87, 60–69.
- Hearty, P.J., Kaufman, D.S., 2000. Whole-rock aminostratigraphy and Quaternary sea-level history of the Bahamas. *Quat. Res.* 54 (2), 163–173.
- Huntley, D.J., Hutton, J.T., Prescott, J.R., 1994. Further thermoluminescence dates from the dune sequence in the southeast of South Australia. *Quat. Sci. Rev.* 13, 201–207.
- Hubyers, P., Wunsch, C., 2004. A depth-derived Pleistocene age model: uncertainty estimates, sedimentation variability, and nonlinear climate change. *Paleoceanography* 19. <http://dx.doi.org/10.1029/2002PA000857>.
- Ivins, E.R., Dokka, R.K., Blom, R.G., 2007. Post-glacial sediment load and subsidence in coastal Louisiana. *Geophys. Res. Lett.* 34.
- James, T.S., Clague, J.J., Wang, K., Hutchinson, I., 2000. Postglacial rebound at the northern Cascadia subduction zone. *Quat. Sci. Rev.* 19, 1527–1541.
- Kaufman, A., Broecker, W.S., Ku, T.L., Thurber, D.L., 1971. The status of U-series methods of mollusk dating. *Geochim. Cosmochim. Acta* 35 (11), 1155–1183.
- Kelsey, H.M., Bockheim, J.G., 1994. Coastal landscape evolution as a function of eustasy and surface uplift rate, Cascadia margin, southern Oregon. *Geol. Soc. Am. Bull.* 106, 840–854. [http://dx.doi.org/10.1130/0016-7606\(1994\)106<0840:CLEA AF>2.3.CO;2](http://dx.doi.org/10.1130/0016-7606(1994)106<0840:CLEA AF>2.3.CO;2).
- Kelsey, H.M., Ticknor, R.L., Bockheim, J.G., Mitchell, C.E., 1996. Quaternary upper plate deformation in coastal Oregon. *Geol. Soc. Am. Bull.* 108, 843–860. [http://dx.doi.org/10.1130/0016-7606\(1996\)108<0843:QUPDIC>2.3.CO;2](http://dx.doi.org/10.1130/0016-7606(1996)108<0843:QUPDIC>2.3.CO;2).
- Kendall, R.A., Mitrovica, J.X., Milne, G.A., 2005. On post-glacial sea level – II: numerical formulation and comparative results on spherically symmetric models. *Geophys. J. Int.* 161, 679–706.
- Kennedy, G.L., Lajoie, K.R., Wehmiller, J.F., 1982. Aminostratigraphy and faunal correlations of late Quaternary marine terraces, Pacific coast, USA. *Nature* 299, 545–547. <http://dx.doi.org/10.1038/299545a0>.
- Kern, J.P., Rockwell, T.K., 1992. Chronology and deformation of quaternary marine shorelines, San Diego county, California. In: Fletcher, C.H., Wehmiller, J.F. (Eds.), *Quaternary Coasts of the United States: Marine and Lacustrine Systems*. Society for Sedimentary Geology (SEPM) Special Publication 48, pp. 377–382.
- Kopp, R.E., Simons, F.J., Mitrovica, J.X., Malof, A.C., Oppenheimer, M., 2009. Probabilistic assessment of sea level during the Last Interglacial stage. *Nature* 462, 863–867.
- Ku, T.L., Kern, J.P., 1974. Uranium-series age of the upper Pleistocene Nestor terrace, San Diego, California. *Geol. Soc. Am. Bull.* 85, 1713–1716.
- Lambeck, K., Chappell, J., 2001. Sea level change through the last glacial cycle. *Science* 292, 679–686.
- Lambeck, K., Smith, C., Johnston, P., 1998. Sea-level change, glacial rebound and mantle viscosity for northern Europe. *Geophys. J. Int.* 134, 102–144.
- Latychev, K., Mitrovica, J., Tromp, J., Tamisea, M., Komatsitsch, D., Christara, C., 2005. Glacial isostatic adjustment on 3-D Earth models: a finite-volume formulation. *Geophys. J. Int.* 161, 421–444.
- Lighty, R.G., Macintyre, I.G., Stuckenrath, R., 1982. Acropora palmata reef framework: a reliable indicator of sea level in the western Atlantic for the past 10,000 years. *Coral Reefs* 1, 125–130.
- Lisicki, L.E., Raymo, M.E., 2005. A Pliocene–Pleistocene stack of 57 globally distributed benthic  $\delta^{18}\text{O}$  records. *Paleoceanography* 20 (1).
- Ludwig, K.R., Muhs, D.R., Simmons, K.R., Halley, R.B., Shinn, E.A., 1996. Sea-level records at ~80 ka from tectonically stable platforms: Florida and Bermuda. *Geology* 24, 211–214.
- Marquardt, C., Lavenu, A., Ortlieb, L., Godoy, E., Comte, D., 2004. Coastal neotectonics in Southern Central Andes: uplift and deformation of marine terraces in Northern Chile (27°S). *Tectonophysics* 394, 193–219.
- McNelly, G.W., Kelsey, H.M., 1990. Late Quaternary tectonic deformation in the Cape Arago-Bandon region of coastal Oregon as deduced from wave-cut platforms. *J. Geophys. Res.* 95, 6699–6713. <http://dx.doi.org/10.1029/JB095iB05p06699>.
- McKay, N.P., Overpeck, J.T., Otto-Bliesner, B.L., 2011. The role of ocean thermal expansion in Last Interglacial sea level rise. *Geophys. Res. Lett.* 38, L14605.
- Merritts, D., Bull, W.B., 1989. Interpreting Quaternary uplift rates at the Mendocino triple junction, northern California, from uplifted marine terraces. *Geology* 17, 1020–1024. [http://dx.doi.org/10.1130/0091-7613\(1989\)017<1020:IQURAT>2.3.CO;2](http://dx.doi.org/10.1130/0091-7613(1989)017<1020:IQURAT>2.3.CO;2).
- Mesolella, K.J., Matthews, R.K., Broecker, W.S., Thurber, D.L., 1969. The astronomical theory of climatic change: Barbados data. *J. Geol.* 77, 250–274.
- Mesolella, K.J., Sealy, H.A., Matthews, R.K., 1970. Facies geometries within pleistocene reefs of Barbados, West Indies. *AAPG Bull.* 54, 1899–1917.
- Milankovitch, M., 1938. Die chronologie des Pleistocans. *Bull. Acad. Sci. Math. Nat. Belg.* 4, 49.
- Milne, G.A., Mitrovica, J.X., 1996. Postglacial sea-level change on a rotating Earth: first results from a gravitationally self-consistent sea-level equation. *Geophys. J. Int.* 126 (3), F13–F20.
- Milne, G.A., Mitrovica, J.X., 1998. Postglacial sea level change on a rotating Earth. *Geophys. J. Int.* 133, 1–10.
- Mitrovica, J.X., Forte, A.M., 2004. A new inference of mantle viscosity based upon joint inversion of convection and glacial isostatic adjustment data. *Earth Planet. Sci. Lett.* 225, 177–189.
- Mitrovica, Milne, G.A., 2003. On post-glacial sea level: 1. General Theory. *Geophys. J. Int.* 154, 253–267.
- Mitrovica, J.X., Wahr, J., Matsuyama, I., Paulson, A., 2005. The rotational stability of an ice-age Earth. *Geophys. J. Int.* 161, 491–506.
- Mix, A.C., 1987. The oxygen-isotope record of glaciation. In: Ruddiman, W.F., Wright, H.E. (Eds.), *North America and Adjacent Oceans during the Last Deglaciation: the Geology of North America*, vols. K-3. Geological Society of America, Boulder, CO, pp. 111–135.
- Mueller, K., Kier, G., Rockwell, T., Jones, C.H., 2009. Quaternary rift flank uplift of the Peninsular Ranges in Baja and southern California by removal of mantle lithosphere. *Tectonics* 28, TC5003. <http://dx.doi.org/10.1029/2007TC002227>.
- Muhs, D.R., Kelsey, H.M., Miller, G.H., Kennedy, G.L., Whelan, J.F., Mcnelly, G.W., 1990. Age estimates and uplift rates for late Pleistocene marine terraces: Southern Oregon portion of the Cascadia forearc. *J. Geophys. Res.* 95, 6685–6698. <http://dx.doi.org/10.1029/JB095iB05p06685>.
- Muhs, D.R., Miller, G.H., Whelan, J.F., Kennedy, G.L., 1992. Aminostratigraphy and oxygen isotope stratigraphy of marine-terrace deposits, Palos Verdes Hills and San Pedro areas, Los Angeles county, California. In: Fletcher, C.H., Wehmiller, J.F. (Eds.), *Quaternary Coasts of the United States: Marine and Lacustrine Systems*. Society for Sedimentary Geology (SEPM) Special Publication 48, pp. 363–376.
- Muhs, D.R., Szabo, B.J., 1994. New uranium-series ages of the Waimanalo Limestone, Oahu, Hawaii: implications for sea level during the last interglacial period. *Mar. Geol.* 118, 315–326.
- Muhs, D.R., Kennedy, G.L., Rockwell, T.K., 1994. Uranium-series ages of marine terrace corals from the Pacific coast of North America and implications for last-interglacial sea level history. *Quat. Res.* 42 (1), 72–87.
- Muhs, D.R., Simmons, K.R., Kennedy, G.L., Rockwell, T.K., 2002a. The last interglacial period on the Pacific Coast of North America: timing and paleoclimate. *Geol. Soc. Am. Bull.* 114, 569–592.
- Muhs, D.R., Simmons, K.R., Steinke, B., 2002b. Timing and warmth of the Last Interglacial period: new U-series evidence from Hawaii and Bermuda and a new fossil compilation for North America. *Quat. Sci. Rev.* 21, 1355–1383.
- Muhs, D.R., Simmons, K.R., Kennedy, G.L., Ludwig, K.R., Groves, L.T., 2006. A cool eastern Pacific Ocean at the close of the last interglacial complex. *Quat. Sci. Rev.* 25, 235–262. <http://dx.doi.org/10.1016/j.quascirev.2005.03.014>.
- Muhs, D.R., Simmons, K.R., Schumann, R.R., Groves, L.T., Mitrovica, J.X., Laurel, D., 2012. Sea-level history during the Last Interglacial complex on San Nicolas Island, California: implications for glacial isostatic adjustment processes, paleo-zoogeography and tectonics. *Quat. Sci. Rev.* 37, 1–25.
- Muhs, D.R., Simmons, K.R., Schumann, R.R., Groves, L.T., DeVogel, S.B., Minor, S.A., Laurel, D., 2014. Coastal tectonics on the eastern margin of the Pacific Rim: late quaternary sea-level history and uplift rates, channel islands national park, California, USA. *Quaternary Sci. Rev.* 105, 209–238. <http://dx.doi.org/10.1016/j.quascirev.2014.09.017>.
- Muhs, D.R., Simmons, K.R., Groves, L.T., McGeehan, J.P., Schumann, R.R., Agenbroad, L.D., 2015. Late Quaternary sea-level history and the antiquity of mammoths (*Mammuthus exilis* and *Mammuthus columbi*), Channel Islands National Park, California, USA. *Quat. Res.* 83, 502–521.
- Murray-Wallace, C.V., 2002. Pleistocene coastal stratigraphy, sea-level highstands and neotectonism of the southern Australian passive continental margin—a review. *J. Quat. Sci.* 17, 469–489.
- Murray-Wallace, C.V., Woodroffe, C.D., 2014. *Quaternary Sea-level Changes: a Global Perspective*. Cambridge University Press.
- Neumann, A.C., Moore, W.S., 1975. Sea level events and Pleistocene coral ages in the northern Bahamas. *Quat. Res.* 5, 215–224.
- Omura, A., Maeda, Y., Kawana, T., Siriring, F.P., Berdin, R.D., 2004. U-series dates of Pleistocene corals and their implications to the paleo-sea levels and the vertical

- displacement in the Central Philippines. *Quat. Int.* 115, 3–13.
- Ota, Y., Omura, A., 1992. Contrasting styles and rates of tectonic uplift of coral reef terraces in the Ryukyu and Daito Islands, southwestern Japan. *Quat. Int.* 15, 17–29.
- Parham, P.R., Riggs, S.R., Culver, S.J., Mallinson, D.J., Jack Rink, W., Burdette, K., 2013. Quaternary coastal lithofacies, sequence development and stratigraphy in a passive margin setting, North Carolina and Virginia, USA. *Sedimentology* 60, 503–547.
- Peltier, W.R., 2004. Global glacial isostasy and the surface of the ice-age Earth: the ICE-5G (VM2) model and GRACE. *Ann. Rev. Earth Planet. Sci.* 32, 111–149.
- Perg, L.A., Anderson, R.S., Finkel, R.C., 2001. Use of a new  $^{10}\text{Be}$  and  $^{26}\text{Al}$  inventory method to date marine terraces, Santa Cruz, California, USA. *Geology* 29, 879–882. [http://dx.doi.org/10.1130/0091-7613\(2001\)029<0879:UOANBA>2.0.CO;2](http://dx.doi.org/10.1130/0091-7613(2001)029<0879:UOANBA>2.0.CO;2).
- Pirazzoli, P.A., 1986. Marine notches. In: *Sea-level Research*. Springer, Netherlands, pp. 361–400.
- Potter, E.-K., Lambeck, K., 2003. Reconciliation of sea-level observations in the Western Atlantic during the last glacial cycle. *Earth Planet. Sci. Lett.* 217, 171–181.
- Potter, E.-K., Esat, T.M., Schellmann, G., Radtke, U., Lambeck, K., McCulloch, M.T., 2004. Suborbital-period sea-level oscillations during marine isotope substages 5a and 5c. *Earth Planet. Sci. Lett.* 225, 191–204.
- Raymo, M.E., Mitrovica, J.X., 2012. Collapse of polar ice sheets during the stage 11 interglacial. *Nature* 483, 453–456.
- Richards, D.A., Smart, P.L., Edwards, R.L., 1994. Maximum sea levels for the last glacial period from U-series ages of submerged speleothems. *Nature* 367, 357–360.
- Ringor, C.L., Omura, A., Maeda, Y., 2004. Last interglacial sea level changes deduced from coral reef terraces in southwest Bohol, central Philippines. *Quat. Res.* 46, 401–416.
- Ritsema, J., Deuss, A., van Heijst, H.J., Woodhouse, J.H., 2011. S4ORTS: a degree-40 shear-velocity model for the mantle from new Rayleigh wave dispersion, teleseismic traveltimes and normal-mode splitting function measurements. *Geophys. J. Int.* 184, 1223–1236.
- Rockwell, T.K., Muhs, D.R., Kennedy, G.L., Hatch, M.E., Wilson, S.H., Klinger, R.E., 1989. In: Abbott, P.L. (Ed.), *Uranium-series Ages, Faunal Correlations and Tectonic Deformation of Marine Terraces within the Agua Blanca Fault Zone at Punta Banda, Northern Baja California, Mexico*. Geologic Studies in Baja California: Los Angeles, California, Pacific Section, Society of Economic Paleontologists and Mineralogists, pp. 1–16.
- Rockwell, T.K., Nolan, F., Johnson, D.L., Patterson, R.H., 1992. Ages and deformation of marine terraces between Point conception and Gaviota, western transverse ranges, California. In: Fletcher, C.H., Wehmiller, J. (Eds.), *Quaternary Coast of the United States: Marine and Lacustrine Systems*. Society for Sedimentary Geology (SEPM) Special Publication 48, pp. 333–341.
- Rovere, A., Raymo, M.E., Vacchi, M., Lorscheid, T., Stocchi, P., Gómez-Pujol, L., Harris, D.L., Casella, E., O'Leary, M.J., Hearty, P.J., 2016. The analysis of last interglacial (MIS 5e) relative sea-level indicators: reconstructing sea-level in a warmer world. *Earth Sci. Rev.* 159, 404–427.
- Shackleton, N.J., 2000. The 100,000-year ice-age cycle identified and found to lag temperature, carbon dioxide, and orbital eccentricity. *Science* 289, 1897–1902.
- Shakun, J.D., Lea, D.W., Lisiecki, L.E., Raymo, M.E., 2015. An 800-kyr record of global surface ocean  $\delta^{18}\text{O}$  and implications for ice volume-temperature coupling. *Earth Planet. Sci. Lett.* 426, 58–68.
- Sherman, C.E., Fletcher, C.H., Rubin, K.H., 1999. Marine and meteoric diagenesis of Pleistocene carbonates from a nearshore submarine terrace, Oahu, Hawaii. *J. Sediment. Res.* 69, 1083–1097.
- Sherman, C.E., Fletcher, C.H., Rubin, K.H., Simmons, K.R., Adey, W.H., 2014. Sea-level and reef accretion history of Marine Oxygen Isotope Stage 7 and late Stage 5 based on age and facies of submerged late Pleistocene reefs, Oahu, Hawaii. *Quat. Res.* 81, 138–150.
- Siddall, M., Rohling, E.J., Almogi-Labin, A., Hemleben, C., Meischner, D., Schmelzer, I., Smeed, D.A., 2003. Sea-level fluctuations during the last glacial cycle. *Nature* 423, 853–858.
- Siddall, M., Rohling, E.J., Thompson, W.G., Waelbroeck, C., 2008. Marine isotope stage 3 sea level fluctuations: data synthesis and new outlook. *Rev. Geophys.* 46 (4).
- Simms, A.R., Lambeck, K., Purcell, A., Anderson, J.B., Rodriguez, A.B., 2007. Sea-level history of the Gulf of Mexico since the last glacial maximum with implications for the melting history of the Laurentide ice sheet. *Quat. Sci. Rev.* 26, 920–940.
- Simms, A.R., DeWitt, R., Rodriguez, A.B., Lambeck, K., Anderson, J.B., 2009. Revisiting marine isotope stage 3 and 5a (MIS3–5a) sea levels within the northwestern Gulf of Mexico. *Glob. Planet. Change* 66, 100–111.
- Simms, A.R., Rouby, H., Lambeck, K., 2015. Marine terraces and rates of vertical tectonic motion: the importance of glacio-isostatic adjustment along the Pacific coast of central North America. *Geol. Soc. Am. Bull.* 128, 81–93.
- Szabo, B.J., 1985. Uranium-series dating of fossil corals from marine sediments of southeastern United States Atlantic Coastal Plain. *Geol. Soc. Am. Bull.* 96, 398–406.
- Szabo, B.J., Rosholt, J.N., 1969. Uranium-series dating of Pleistocene molluscan shells from southern California—an open system model. *J. Geo Phys. Res.* 74, 3253–3260. <http://dx.doi.org/10.1029/JB074i012p03253>.
- Toscano, M.A., Lundberg, J., 1999. Submerged Late Pleistocene reefs on the tectonically-stable SE Florida margin: high-precision geochronology, stratigraphy, resolution of Substage 5a sea-level elevation, and orbital forcing. *Quat. Sci. Rev.* 18, 753–767.
- Vacher, H.L., Hearty, P., 1989. History of stage 5 sea level in Bermuda: review with new evidence of a brief rise to present sea level during substage 5a. *Quat. Sci. Rev.* 8, 159–168.
- Waelbroeck, C., Labeyrie, L., Michel, E., Cl Duplessy, J., McManus, J.F., Lambeck, K., Balbon, E., Labracherie, M., 2002. Sea-level and deep water temperature changes derived from benthic foraminifera isotopic records. *Quat. Sci. Rev.* 21, 295–305.
- Wainer, K.A., Rowe, M.P., Thomas, A.L., Mason, A.J., Williams, B., Tamisiea, M.E., Williams, F.H., Düsterhus, A., Henderson, G.M., 2017. Speleothem evidence for MIS 5c and 5a sea level above modern level at Bermuda. *Earth Planet. Sci. Lett.* 457, 325–334.
- Wehmiller, J.F., Simmons, K.R., Cheng, H., Edwards, R.L., Martin-McNaughton, J., York, L.L., Krantz, D.E., Shen, C.C., 2004. Uranium-series coral ages from the US Atlantic Coastal Plain—the “80ka problem” revisited. *Quat. Int.* 120, 3–14.